Processing and Properties of Amorphous NiW Reinforced Crystalline Ni Matrix Composites

Charles Alexander Wensley

Thesis submitted to the faculty of the
Virginia Polytechnic Institute and State University
in partial fulfillment of the requirements for the degree of

Master of Science

in

Materials Science and Engineering

Dr. Alex Aning, Co-chair
Dr. Stephen Kampe, Co-chair
Dr. William Reynolds

December 16, 2005
Virginia Tech
Blacksburg, VA

Keywords: Metal Matrix Composites, Amorphous, Particulate Reinforcement, Mechanical Alloying

Processing and Properties of Amorphous NiW Reinforced Crystalline Ni Matrix Composites

Charles Wensley

ABSTRACT

Metal Matrix Composites (MMCs) are used as structural materials because of their ability to have a combination of high strength and good ductility. A common problem with MMCs utilizing vastly different materials is the difficulty in forming a strong matrix/reinforcement interface without suffering extensive dissolution, debonding, or chemical reactions between the components. In this work, a nickel base amorphous particulate reinforced crystalline nickel matrix composite is processed. The reinforcement, an equimolar NiW amorphous powder, was synthesized using the mechanical alloying process. The amorphous and crystalline nickel powders were blended in varying volume fractions and then consolidated using hot-isostatic pressing (HIP). This work reveals that the amorphous NiW reinforcement provides strength and hardness to the ductile Ni matrix while simultaneously maintaining a strong interfacial bond due to the similar chemistry of the two components. The strengthening achieved in the composite is attributed to the particulate/matrix boundary strengthening.

ACKNOWLEDGEMENTS

I would like to start by thanking my advisor Dr. Alex Aning for his knowledge and guidance in support of my research, and for sitting through all of my presentations. I would also like to thank Dr. Stephen Kampe for his quick replies to my questions and for his insightful composite knowledge.

I'd like to thank Dr. William Reynolds for answering several left-field questions and also for being on my committee.

To Dr. Jeff Schultz, I would like to extend a very warm appreciation for his help in every aspect of my research. He has taught me more about being an engineer than anyone.

Lastly, I'd like to thank David Berry and everyone in the Kamposites group for their help and/or humor.

TABLE OF CONTENTS

Chapter One – Introduction 1
Chapter Two – Historical Background 3
2.1 MMCs 3
2.2 MMC Interfaces 4
2.3 Mechanical Alloying (MA) 7
2.4 Amorphous Metals 8
2.4.1 Synthesis of Amorphous Metals 8
2.4.2 Synthesis of Amorphous Metals by Mechanical Alloying 9
2.5 Amorphous Reinforced MMCs 11
2.6 Consolidation 12
Chapter Three – Experimental Procedures 14
3.1 Production of the Reinforcement Particles 14
3.2 Homogenization of Amorphous and Crystalline Powders 14
3.3 Consolidation of Powders 15
3.4 Analysis of Composite Samples 17
Chapter Four – Experimental Results 19
4.1 Analysis of Reinforcement Powder Particles 19
4.1.1 X-ray Diffraction Results 19
4.1.2 Particle Size 20
4.2 Analysis of Composite Samples 20
4.2.1 X-ray Diffraction Results 20
4.2.2 Microscopy 21
4.2.3 Compression Tests 23
4.2.4 Vickers Hardness Tests 25
4.2.5 Density and Porosity Calculations 27
Chapter Five – Discussion 30
5.1 ΔCTE Strengthening 30
5.2 Orowan Strengthening 32
5.3 Boundary Strengthening 33
5.4 $L_{e\text{-}e}$ Estimation using Image Analysis 34
5.5 Calculated Strengthening Contributions 35
Chapter Six – Conclusions 40
Chapter Seven – Future Work 41
References 42
Appendix A: Composite Yield Stress at 0.2% Strain Offset 45
Appendix B: Vickers Macro-hardness Measurements on Composite Samples 45
Appendix C: Detailed Explanation of $L_{e\text{-}e}$ Calculations with ImageJ and Mathematica 46
Appendix D: Mathematica Program to Estimate $L_{e\text{-}e}$ 49
Appendix E: $L_{e\text{-}e}$ Values Estimated by Mathematica for Each Composite 50

LIST OF FIGURES

Figure 1. Schematic of composite strengthening as a function of reinforcement size, shape, and volume fraction. The left illustration shows matrix dominated strengthening. The right illustration shows stiffening and strengthening gained from load transfer to high aspect ratio reinforcement [3]. 4
Figure 2. Contact angle θ and the surface energies γ for a liquid drop on a solid surface....5
Figure 3. Early stages of milling and the start of a lamellar structure, MA 1 hour 7
Figure 4. Intermediate stage where the lamellar structure is being refined, MA 5 hours....7
Figure 5. Miedema thermodynamic theory calculations of the formation energies of several Ni alloy systems. 11
Figure 6. Diagram showing subgrain diameter and boundaries 11
Figure 7. 0 vol. % - Outside can diameter shrinkage vs. temperature 15
Figure 8. 0 vol. % - Outside can diameter shrinkage and temperature vs. time 15
Figure 9. 0 vol. % - Pressure and temperature profile seen by can....15
Figure 10. 10 vol. % - Outside can diameter shrinkage vs. temperature 15
Figure 11. 10 vol. % - Outside can diameter shrinkage and temperature vs. time 16
Figure 12. 10 vol. % - Pressure and temperature profile seen by can....16
Figure 13. 25 vol. % - Outside can diameter shrinkage vs. temperature 16
Figure 14. 25 vol. % - Outside can diameter shrinkage and temperature vs. time 16
Figure 15. 25 vol. % - Pressure and temperature profile seen by can....16
Figure 16. 45 vol. % - Outside can diameter shrinkage vs. temperature 16
Figure 17. 45 vol. % - Outside can diameter shrinkage and temperature vs. time 17
Figure 18. 45 vol. % - Pressure and temperature profile seen by can....17
Figure 19. XRD patterns of un-milled and milled NiW 19
Figure 20. XRD patterns of 10, 25, and 45 vol. % reinforcement composites. Nickel peaks become shorter and broader with increasing reinforcement. 20
Figure 21. Optical micrograph of a 0 vol. % reinforcement sample – pure nickel....21
Figure 22. Optical micrograph of a 10 vol. % reinforcement composite 21
Figure 23. Optical micrograph of a 25 vol. % reinforcement composite 21
Figure 24. Optical micrograph of a 45 vol. % reinforcement composite 21
Figure 25. Highly dense pure nickel sample....22
Figure 26. Random particulate dispersion in 10 vol. % reinforcement composite....22
Figure 27. Random particulate dispersion in 25 vol. % reinforcement composite....22
Figure 28. Random particulate dispersion in 45 vol. % reinforcement composite....22
Figure 29. Sub-particles embedded in a reinforcement particle of a 10 vol. % reinforcement composite 23
Figure 30. Sub-particles embedded in a reinforcement particle of a 25 vol. % reinforcement composite 23
Figure 31. Compression test results for the three composites and the pure nickel compact 23
Figure 32. Plot of average yield stress vs. reinforcement volume percent 24
Figure 33. Particulate fractures in post-compression 10 vol. % reinforcement composite – aligned with compression in vertical axis 25
Figure 34. Particulate fractures in post-compression 25 vol. % reinforcement composite – aligned with compression in vertical axis 25

Figure 35. Particulate fractures in post-compression 45 vol. % reinforcement composite – aligned with compression in vertical axis 25
Figure 36. Angular view of fracture surface also showing second failure initiation in 45 vol. % reinforcement composite 25
Figure 37. Plot showing average composite Vickers macro-hardness increase with higher volume fraction of reinforcement 27
Figure 38. Apparent density measurements for composite samples using three different techniques 29
Figure 39. Orowan process of a dislocation bowing around a particle and leaving a dislocation loop 32
Figure 40. Calculated strengthening contributions to MMCs 36
Figure 41. Plot of yield strength versus inverse square root of reinforcement particle spacing 37
Figure 42. Plot of Vickers macro-hardness versus inverse square root of reinforcement particle spacing 38
Figure 43. Plot of yield strength versus Vickers macro-hardness for the pure nickel sample and the three composites 39
Figure 44. SEM image cropped 46
Figure 45. Binary/Threshold 1 46
Figure 46. Binary/Threshold 2 47
Figure 47. Mask of Figure 46 47
Figure 48. Example plot-profile graph of a line drawn on an SEM image using ImageJ 48

LIST OF TABLES

Table 1. Four composite blends with differing reinforcement volumes 14
Table 2. Averages of Vickers macro-hardness measurements on composite samples 26
Table 3. Density and porosity values calculated using different analysis techniques 29
Table 4. Thermal expansion values for nickel and tungsten [51] 31
Table 5. Average calculated reinforcement particle spacing 35

Chapter One – Introduction

Metal Matrix Composites (MMCs) often have a relatively ductile metal matrix phase and a significantly harder reinforcement material [1] like ceramics or refractory metals. The matrix holds the reinforcement material together and provides ductility while the reinforcement imparts strength and stiffness to the composite. A common problem with MMCs is the difficulty in creating a strong matrix/reinforcement interface without suffering extensive dissolution, debonding, or chemical reactions [2-4]. A proposed solution is the use of a reinforcement material which is similar in chemistry to the matrix. This research is aimed at creating a MMC reinforced with Ni-W amorphous particulates which should have a chemical similarity to the crystalline nickel matrix [5].

Many unique properties of amorphous metals have been demonstrated including higher hardness, higher strength, and better corrosion resistance than their crystalline counterparts [6]. These qualities make amorphous metals ideal for use as a reinforcement phase in MMCs. However, it is important to note that amorphous metals are metastable, and can recrystallize when kinetically favorable.

Numerous processes have been developed to fabricate amorphous metals such as rapid quenching [7], irradiation [8, 9], solid-state amorphization reaction [10], and mechanical alloying. Mechanical alloying (MA) is a solid-state mechanical deformation process which can produce an amorphous alloy powder from elemental powders [11-14]. There are three major types of MA devices namely vibratory ball mill, attritor, and tumbler ball mill. In this research, the SPEX 8000 mill, a vibratory ball mill was selected to synthesize the Ni-W amorphous powder because it is the most energetic of the mills.

Metal powders may be consolidated in several ways. These include cold pressing, liquid and solid-phase sintering, hot-uniaxial [15] and hot-isostatic pressing [16], warm rolling [17], warm extrusion [18], shock compression [19-22], and spark plasma sintering [23, 24]. However, caution must be exercised during the consolidation of samples containing amorphous powder. Pressure and/or temperature can crystallize amorphous metals if high enough. From research conducted by Kawamura and others, it has been shown that amorphous metal powder can be formed into a solid compact using hot pressing [25]. Hot-isostatic pressing (HIP) was used to consolidate the metal powder in these experiments.

By synthesizing an amorphous Ni-W powder using MA and mixing and consolidating it with crystalline Ni powder, a MMC is formed. Multiple samples were created to show the effect of the amorphous powder volume fraction on the density, strength, and hardness. This research aims to show the benefits of using amorphous metal alloys as a reinforcement material in metal matrix composites.

Chapter Two – Historical Background

2.1 MMCs

Composite materials have been around for a long time. It is known that some of the earliest composites were made from mud and straw. A broad definition for a composite is: a combination of two components separated by a distinct interface, thermodynamically irreversible, and has properties which can be 'engineered' using composite principles [26]. Composite principles are known material responses as a function of variables such as reinforcement volume fraction, reinforcement size and shape, and interface strength based on material and interface mechanics equations. Specifically metal matrix composites have been extensively fabricated and studied. This is in part because it is possible to create a material which has a useful combination of the toughness and impact resistance of a ductile material and the strength and hardness of a brittle material.

The first MMCs were dispersion strengthened alloys created in the 1950's. The strengthening mechanism is the impediment of dislocation motion using small volume fractions (<15%) of precipitates or inclusions less than 1 micron in size. This strengthening is predicted by work hardening due to Orowan looping [27]. In the 1960's, a lot of research was put forth into fiber reinforced MMCs to examine strengthening by shear load transfer [3]. The primary matrix role in these composites is to transfer the applied load to the fibers using the fiber/matrix interface. However continuous fiber reinforced composites have high costs and production limitations. Other discontinuous reinforcements such as short fibers, whiskers, and particulates were extensively studied during the 1980's. They have several attractive benefits such as low cost, high workability, and better mechanical performance than unreinforced alloys [28]. In these discontinuous reinforced composites, the load bearing is between the extremes of the dispersion strengthened and fiber strengthened composites. The load is shared between the reinforcement and the matrix in differing proportions depending on the reinforcement type and alignment. The left graph in Figure 1 shows composite matrix strengthening from different means as a function of the reinforcement diameter. The right graph shows composite strengthening and stiffening gained from shear load transfer as a function of reinforcement aspect ratio.

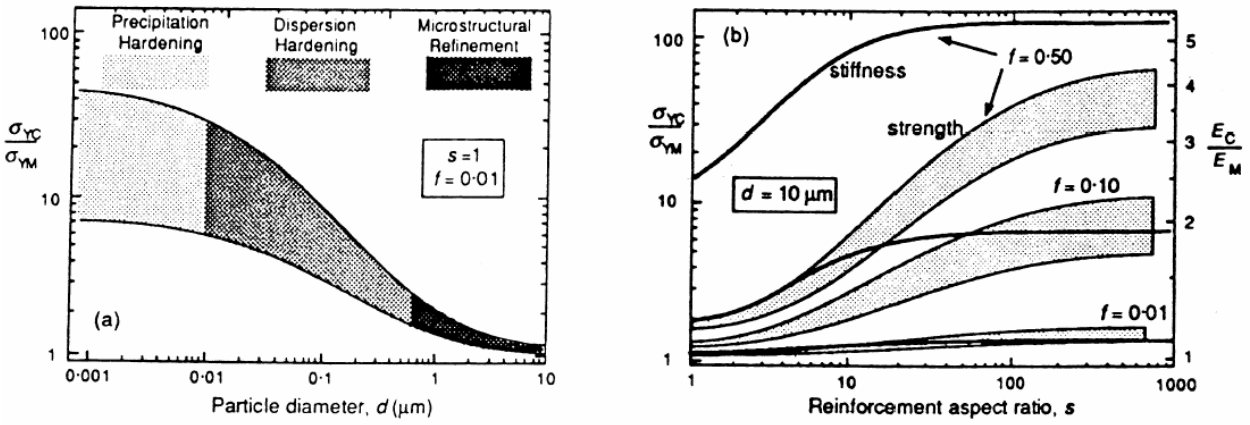

Figure 1. Schematic of composite strengthening as a function of reinforcement size, shape, and volume fraction. The left illustration shows matrix dominated strengthening. The right illustration shows stiffening and strengthening gained from load transfer to high aspect ratio reinforcement [3].

Discontinuous particulate reinforced MMCs usually have 1-100μm equiaxed shaped reinforcement in 5-40% volume fractions. Because the reinforcement has a small aspect ratio, the strengthening mechanism is not reliant upon shear load transfer but more similar to the dislocation strengthening in dispersion reinforcement [3]. Strengthening occurs when the dispersed particles resist matrix deformation by mechanical restraint. When loaded, the softer matrix is restrained by the rigid interfaces of the hard reinforcement particles. If the hydrostatic stress component reaches 3-3.5 times the unconstrained matrix yield strength and the particles do not deform, then fracture initiated by particle cracking occurs through the matrix. Cermet materials and cemented carbides exhibit this type of deformation. When dispersed particles do not yield under load, the composite yield strength should be proportional to the inverse root of the interparticle spacing. This has been observed for many steels and cemented carbide materials [29].

2.2 MMC Interfaces

The interface in an MMC is the region between the matrix and reinforcement where some kind of discontinuity occurs. The interface separating these two phases is where there exists a variation in chemical or physical properties [2]. The type of interaction at the interface will greatly influence the mechanical properties of the composite. It is necessary to understand wettability and the modes of interface bonding in MMCs in hopes of creating a material with superior mechanical properties.

Wettability is the term which defines the extent to which a liquid drop will spread on a solid surface, and can be measured by the Sessile Drop Test.

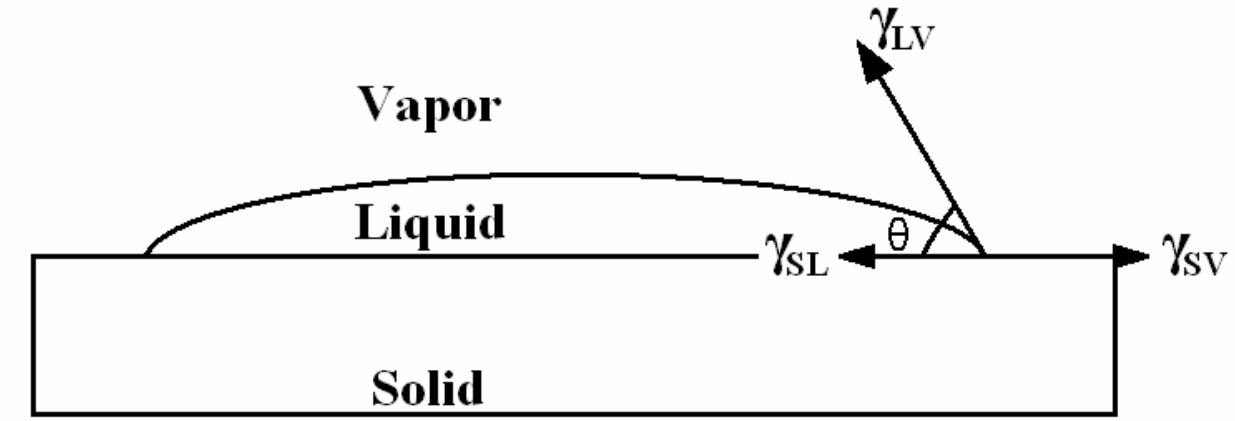

Figure 2. Contact angle θ and the surface energies γ for a liquid drop on a solid surface

The γ's are the surface energies of the liquid/solid, liquid/vapor, and solid/vapor interfaces as illustrated in Figure 2 above. If $\gamma_{SV} > \gamma_{SL}$, then θ will be less than 90° and there exists a net reduction of the systems free energy for the drop to spread and wet the surface of the solid [30].

The wettability notion is important in understanding bonding theory between the matrix and reinforcement in MMCs. Wettability refers to the extent of intimate contact possible at the molecular level. Good bonding is implied when there are uniform atomic or molecular bonds along the interface. In addition, the contact angle is modified by the nature of the surfaces. Adsorbed gases usually raise the contact angle while surface roughness lowers it. While wetting is not systematically measured for all MMCs, the concept is a vital tool to improve the quality of interface bonding [2].

Interface bonding can be achieved by a mechanical bond or by a chemical bond. The mechanical bond can be attained using mechanical interlocking or frictional effects from the thermal contraction of the matrix on the reinforcement [31]. Care must be taken not to damage the reinforcement when modifying the surface for interlocking or surface roughening. Also interface debonding can occur in composites which have residual stresses from thermal contraction if the composite is later exposed to thermal cycling [4]. Mechanical bonding is the weakest bond however and some sort of additional chemical bond is usually preferred.

There are primarily two types of chemical bonds. The first is wetting followed by any degree of dissolution. This chemical bond is an interaction of electrons on an atomic scale and is greatly hindered by the presence of oxide films. If a contact angle between the two phases is less than 90°, then wetting can occur followed by dissolution. It must be noted that if the solubility of the reinforcement in the matrix is significant, then during processing or future heat cycles dissolution can alternatively deteriorate the reinforcement.

The second chemical bond is characterized by the formation of a new chemical compound at the interface by one or more chemical reactions. These bonds can be covalent, ionic, metallic, etc., and are frequently very strong. However it is often observed that the reaction is inadvertent or too strong, and has detrimental effects by forming brittle reaction products [2, 32, 33]. These three interface bonding mechanisms each have strengths and flaws, and must be carefully considered when making an MMC.

To improve composite performance, one must be able to clarify the structure of the interface. Several devices have been used to analyze interfaces in MMCs such as secondary ion mass spectrometry (SIMS), high-energy electron diffraction (HEED), transmission electron spectroscopy (TEM), scanning electron microscopy (SEM) with energy dispersive spectroscopy (EDS), auger electron spectroscopy (AES), Rutherford backscattering spectroscopy (RBS), x-ray photoelectron spectroscopy (XPS), and extended x-ray absorption fine structure spectroscopy (EXAFS) [34]. Each of these techniques can analyze at least one or multiple characteristics of the interface. The important information to gain from the interface bond is the strength, type, and constituting elements. A few of the most useful analysis methods will be discussed. TEM can analyze chemical composition, crystalline state, and has high spatial resolution. XPS and AES are surface techniques which can accurately characterize the chemical state of an element and can easily analyze the distribution of light elements such as oxygen and carbon. XPS can also analyze bonding states which is useful for studying wetting, bonding, and chemical reactivity. EXAFS is well suited for analyzing atomistic scale bonding at MMC interfaces. It can determine the chemical state, chemical interaction, and bond strength at the interface. This is possible by its ability to measure bond types, bond lengths, and atomic coordination [30]. In this research, SEM with EDS is used.

Even with this knowledge of wettability, interface bonding, and analytical techniques, interfaces in MMCs are still being studied. A plausible solution to create a strong chemical inter-

face free of extensive dissolution and chemical reactions is to use a reinforcement which is chemically similar to the matrix. The aim of this research is to have an effective bond between reinforcing amorphous particulates and a matrix based on one of the two constituents of the amorphous phase [5].

2.3 Mechanical Alloying (MA)

Mechanical Alloying is a high energy milling process for the production of composite metallic powders. It utilizes colliding grinding media in a dry atmosphere at room temperature, and occurs by the repeated welding and fracturing of two dissimiliar powder particles. At least one of the two materials must be ductile to act as a binder to hold the particles together. The progress of alloying is defined by microstructural changes, and evolves in three stages. The early stage is characterized by grinding, cold welding, and the initial forming of a lamellar structure as shown in Figure 3. Further flattening, fracturing, and welding of these particles leads to a refinement of the lamellar structure shown in Figure 4. A balance is eventually achieved between the amount of welding and fracturing, and a steady state particle size distribution develops that is a function of the process conditions and the composition of the alloy. While the particle size maintains constant, the refinement rate of the internal structure is logarithmic with time [35]. The last stage is a homogeneous mixture where the lamellae are no longer optically resolvable.

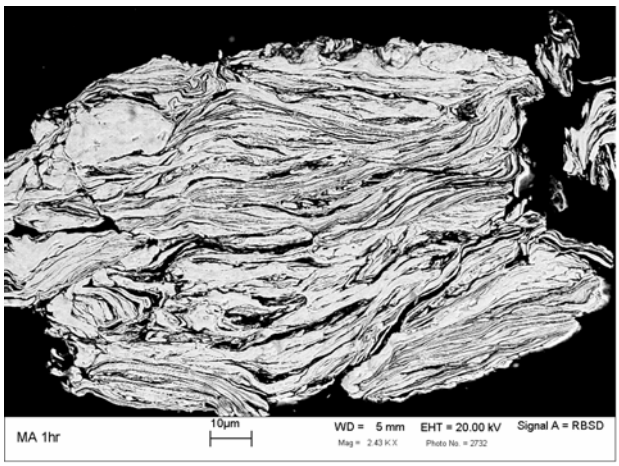

Figure 3. Early stages of milling and the start of a lamellar structure, MA 1 hour

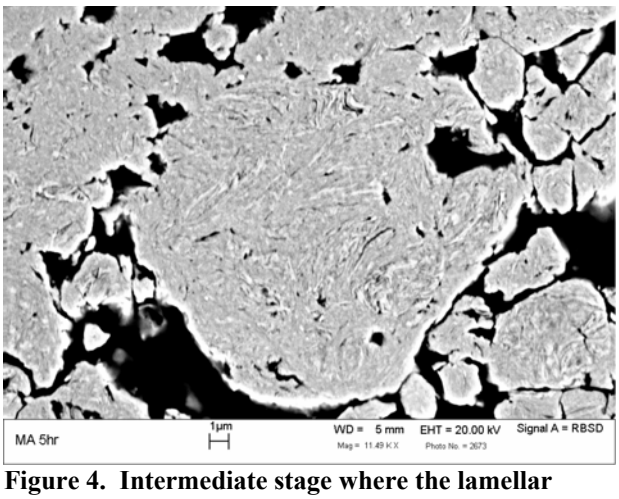

Figure 4. Intermediate stage where the lamellar structure is being refined, MA 5 hours

This process was invented in 1966 by INCO, to develop oxide dispersion strengthened (ODS) nickel-based superalloys. Benjamin used MA to introduce nickel coated oxides into molten alloys to yield strength and stability in high temperature environments. It has since been employed for a variety of uses because MA has many assets such as its capability to mill powder in inert atmospheres, alloy difficult to cast systems, exceed equilibrium solubility limits, form intermetallics, and create amorphous powders [5, 36].

In addition to being able to produce uniform particulate sizes and homogenous microstructures, MA has the capability to alloy powders such as Ti, Mg, and Al in an inert atmosphere like argon. Aluminum for example can oxidize or become pyrophoric if milled in air. MA can also be used to alloy two metals which are difficult to alloy using more traditional methods like casting. Typical examples are Fe/Cu and Fe/W. Iron and copper have a positive enthalpy of mixing and will segregate during cooling [36]. Iron and tungsten are difficult to melt together because of the extremely high T_m of tungsten. However with the energy delivered by MA at room temperature, iron is capable of being alloyed with copper or tungsten. And a unique advantage of MA applied in this research is the ability to create amorphous phases in certain metal alloys. Being a room temperature process, MA can avoid structural changes that might occur in alloys exposed to high temperatures. Amorphization by MA is further discussed in Section 2.4.2.

2.4 Amorphous Metals

Amorphous metals are defined as having no long-range order or periodicity over large atomic distances. Many unique properties are demonstrated in amorphous metals including high hardness, high strength, and excellent corrosion resistance [6]. Amorphous metals however are metastable, and can revert back to a crystalline phase when kinetically favorable.

2.4.1 Synthesis of Amorphous Metals

Several methods have been used to produce amorphous alloys such as rapid quenching, irradiation, solid-state amorphization reaction (SSAR), and mechanical alloying (Section 2.4.2). Rapid quenching a metal from a molten or vapor phase was the first method invented to create amorphous metals. This process requires an incredibly high quench rate to succeed, usually on the order of 10^6-10^{10} K/s. There exist two limiting factors when using rapid solidification to

yield this metastable condition. Primarily, heat transfer considerations require at least one dimension of the specimen to be small, 10-100 μm [37]. Thus the resulting amorphous samples are foils, wires, or powders. Secondly the samples are restricted to narrow compositions around deep eutectics.

Irradiation is a process in which the material is bombarded with fast moving ions, electrons, or neutrons. These particles create defects in the material such as interstitial-vacancy pairs, vacancy loops, and others [8]. The premise is that a critical defect concentration resulting from irradiation destabilizes the crystalline phase, promoting spontaneous transformation of the metal to the amorphous state. The free energy of the defects add to the free energy of the crystalline phase and become larger than the free energy of the amorphous phase [9]. Intermetallics at low temperatures are the best candidates for amorphization as a result of irradiation-induced damage. This is because of their ability to store enthalpy by means of Frenkel pairs, reduction in short and long-range chemical order, and limited migration of defects [38].

SSAR is an amorphization reaction occurring when thin foils of two dissimiliar metals are alternatively stacked and annealed. For example, La and Au foils with 10-60 nm thicknesses have been amorphized at temperatures of 50-80°C [10]. The heat is to assist diffusion but low enough to avoid nucleation and growth of crystalline phases or intermetallics. For this procedure to be successful, two criterion must be met. The heat of mixing of the two metals must be large and negative, to provide a thermodynamic driving force for interdiffusion. In addition, there must exist "anomalous diffusion" whereby one metal must diffuse quickly into the other. This is often seen when the atomic radii sizes of the two elements are different [10]. In some cases, the relative immobility of the larger atoms act as a kinetic constraint to the creation of crystalline compound nuclei [38].

2.4.2 Synthesis of Amorphous Metals by Mechanical Alloying

Mechanical Alloying was first shown to be able to produce amorphous metals in the Ni-Nb system [11]. Subsequent research has demonstrated that many alloy systems are able to form amorphous phases using the MA process [14]. This is a solid-state process similar to SSAR, however it is noted that MA can amorphize systems which do not exhibit a negative heat of mixing and an asymmetric diffusion couple.

Figure 5 shows several enthalpy of mixing curves for different binary alloy systems using Miedema and De chatel model calculations [39].

$$\Delta H_{sol}^{AinB} \approx -P(\Delta\phi^*)^2 + Q(\Delta n_{ws}^{1/3})^2 \quad [1]$$

$$\Delta H_f(A_xB_{1-x}) = x_A \bullet f_B^A \bullet \Delta H_{sol}^{AinB} \quad [2]$$

Equation [1] gives the enthalpy of solution for element A in B. $\Delta\phi$ and Δn_{ws} are the respective electronegativity and electron density differences between the two elements. P and Q are empirical constants. Equation [2] is used to calculate the total enthalpy of formation of the binary alloy. x_A is the atomic concentration of element A, and f_B^A is the degree to which A atoms are in contact with dissimilar atomic neighbors. Modifications made to the Miedema model for amorphous alloys comes from Weeber [40]. Unlike Ni-W, Ni-V has a large negative enthalpy of mixing and can amorphize using SSAR. These binary alloy formation calculations show the chemical driving force towards amorphization, but more is needed to explain how Ni-W amorphizes using MA.

In the Fe-W system, which has a zero heat of mixing, Quan et al and Shen et al concluded the lattice distortion from the supersaturation of tungsten in the iron crystal raised its free energy above that of the amorphous iron phase [12, 41-43]. The Ni-W system can also amorphize from the MA process [44]. It has been speculated that point and lattice defects caused by plastic deformation contribute a 'strain energy', which can raise the free energy of the crystalline phase above that of the amorphous phase [13]. In addition, strain energy is created by subgrain boundary surfaces from the subgrain crystallites created by MA. These subgrain diameters are measured by analyzing crystalline peaks in X-ray diffraction patterns using the Scherrer's formula as seen in Equation [3].

$$d = \frac{0.9 \bullet \lambda}{B \bullet \cos\theta} \quad [3]$$

Here, B is the peak full width at half-maximum (FWHM), λ is the x-ray wavelength, and θ is the Bragg angle. The subgrain diameters are inserted into a simple surface energy equation.

$$\Delta G_{st} = -\frac{4\gamma}{d} \qquad [4]$$

Here, γ is the subgrain boundary energy approximated at 1 J/m^2, d is the subgrain diameter, and ΔG_{st} is the strain free energy. Figure 6 is a sketch of the subgrains and boundaries created by MA.

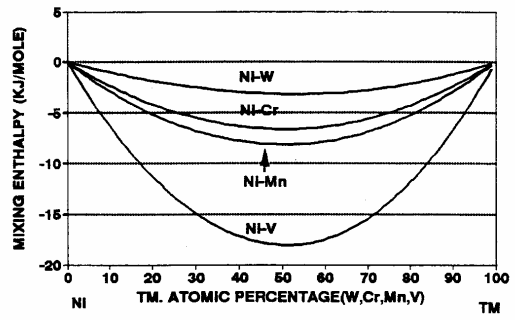

Figure 5. Miedema thermodynamic theory calculations of the formation energies of several Ni alloy systems.

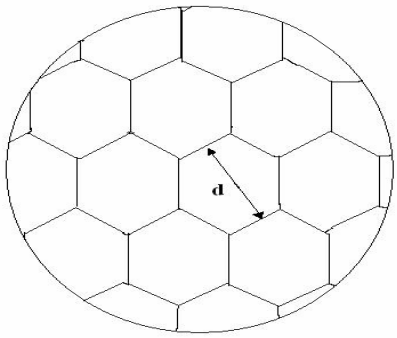

Figure 6. Diagram showing subgrain diameter and boundaries

The summation of the NiW -3 kJ/mole chemical energy and the strain energy created by the subgrain boundaries is near the -18 kJ/mole enthalpy of the NiV binary alloy formation, which can explain how NiW is able to amorphize by MA.

2.5 Amorphous Reinforced MMCs

Amorphous metals have been previously studied for use as reinforcement in ductile matrices because of their high hardness and strength. Some of the first attempts were for use in polyethylene and copper matrices. However, the bonding between the amorphous reinforcement ribbons/wires and the matrices was poor and slippage was evident [45, 46]. In 1982, vacuum hot pressing was shown as a feasible technique to fabricate amorphous reinforced MMCs. A strong bond between the $Ni_{60}Nb_{40}$ amorphous ribbons and Al based matrix was created [47]. Amorphous metal ribbons were later introduced into thermoplastic poly-propylene matrices by sandwich and thin films methods. The sandwich method provided a good interface between the two phases but the thin film method had too much porosity at the interfaces to yield improved performance [48]. More recently in 1994 research done by Stawovy incorporated amorphous Fe-W

into a crystalline iron matrix. He attempted various consolidation techniques: cold pressing, cold pressing – annealing – cold rolling, and HIP. However, through these methods he was not able to achieve a high density. Upon analysis, significant porosity was seen near the reinforcement particles thereby reducing the reinforcement/matrix interface strength. The strength gained in Stawovys' composites by using higher volume fractions of amorphous reinforcement was countered by increasing porosity [49].

2.6 Consolidation

When consolidating amorphous metal powder, its metastable characteristic means that procedures utilizing extreme pressure and temperature will revert the amorphous metal back to its crystalline form. Amorphous metals are less dense than their crystalline counterparts because of random atomic orientation, thus high pressure is a driving force towards crystallization. Processes that have been employed to consolidate metal powders include cold-pressing, liquid and solid-phase sintering, warm extrusion [18], and warm rolling [17]. However, some of these have limitations. Cold-pressing and solid-phase sintering for example often have excess porosity in the final product. Warm extrusion and rolling of thin foils have successfully yielded bulk amorphous alloys of complex four and five component systems with large supercooled liquid regions and high glass forming ability (GFA). These specific alloys allowed for high densification by viscous flow under high pressure while exposed to temperatures below the crystallization (T_x) and yet above the glass transition temperatures (T_g). Three effective amorphous metal powder consolidation procedures are shock compression, spark plasma sintering (SPS), and hot pressing [15]. Carefully executed, these methods yield very dense products. Shock compression is a method developed in 1983 whereby a plate launched at high velocity impacts a container filled with metal powder [22]. As long as the pressure of the impact was sufficient without being excessive there was no crystallization of the amorphous phase, but porosities were in the 7-19% range [19, 21]. Spark Plasma Sintering (SPS) is a newly developed process which makes it possible to sinter high quality materials in short periods by charging the intervals between powder particles with electrical energy and high sintering pressure. This process is very cost efficient and rapid, and can be executed quickly enough to avoid crystalline grain nucleation in amorphous materials [23, 24]. Porosity is often cited as 2%. Unfortunately this technology was not available for this research. Previous research using amorphous Al-based powder has shown the

ability of hot pressing to create a bulk amorphous sample [25]. Hot-isostatic pressing (HIP) is thus used in this research to consolidate the metal powder samples. HIP is a consolidation process whereby metal powder is encapsulated within a ductile metal container or "can" and uniform pressure by a fluid is applied in all three dimensions simultaneously. It is a very effective process for consolidating metal powder, and can achieve very high densities.

Chapter Three – Experimental Procedure

3.1 Production of the Reinforcement Particles

The reinforcement composition was chosen to be Ni – 50 at.% W. Both the nickel and tungsten powder used in the reinforcement were reduced in a hydrogen atmosphere at 500°C for one hour in a Lindberg/Bluem tube furnace, and also stored and milled in an argon atmosphere to prevent oxidation. The equimolar Ni and W mixture was loaded into a SPEX 8000D Mixer/Mill with a charge ratio of 6:1. "Charge Ratio" is defined as the mass ratio of the grinding media to the powder. The milling duration was chosen for 30 hours to ensure a homogenous amorphous phase and because Ni and W crystallite size does not significantly reduce for longer times [44]. X-ray analysis was taken using a Scintag XDS 2000 Diffractometer. Scans measured the diffraction angles from 0-110º using Cu Kα radiation at a speed of 4º per minute. Reinforcement particle size was measured using a Horiba LA-700 Particle Size Analyzer.

3.2 Homogenization of Reinforcement and Matrix Powders

Nickel powder of size -325 mesh was reduced in a hydrogen atmosphere for 1 hour at 500C. This powder serves as the matrix of the composites, and has a density of 8.909 g/cc. The amorphous reinforcement powder was measured to have a density of 13.1377 g/cc using a helium Micromeritics Accupyc 1330 Pycnometer. The two powders were blended to form composites with up to 45 volume percent reinforcement as shown in Table 1.

Table 1. Four composite blends with differing reinforcement volumes

Reinforcement Vol. %	Matrix Vol. %	Reinforcement Weight %	Matrix Weight %
0	100	0.0	100.0
10	90	14.1	85.9
25	75	33.0	67.0
45	55	54.7	45.3

A Szegvari Attritor was used to blend the reinforcement and matrix powders. The agitator speed was set at 300 rpm, and the duration was 3 hours. The mixing can was cooled with a water jacket and was filled with argon flowing at 10-50 ft^3/hr.

3.3 Consolidation of Amorphous and Crystalline Powders

Powder consolidation was done using a Hot Isostatic Press (HIP) operated by Matsys Inc. in Sterling, Virginia. Each powder sample was vacuum encapsulated in a copper can with an internal diameter and length of 0.5 and 2.75 inches, respectively. The pressure and temperature of the HIP was set at 28 ksi and 700ºC for 30 minutes for both the 25 and 45 vol. % reinforcement composites. The zero and 10 vol. % reinforcement composites were held at 600ºC for 12 minutes and 700ºC for 7 minutes, respectively, at 28 ksi as well. The three HIP profiles for each of the four samples are shown in the series of figures below.

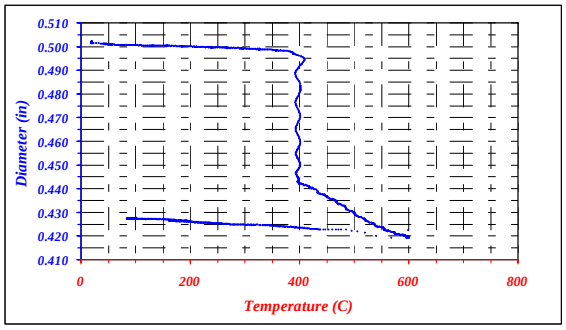

Figure 7. 0 vol. % - Outside can diameter shrinkage vs. temperature

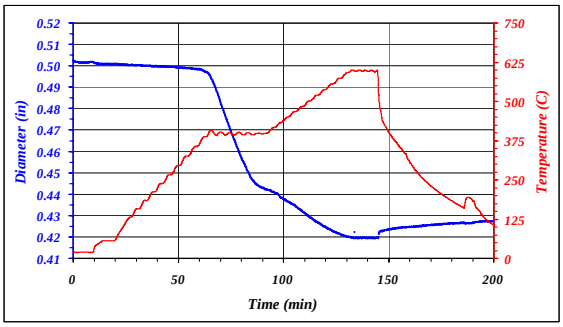

Figure 8. 0 vol. % - Outside can diameter shrinkage and temperature vs. time

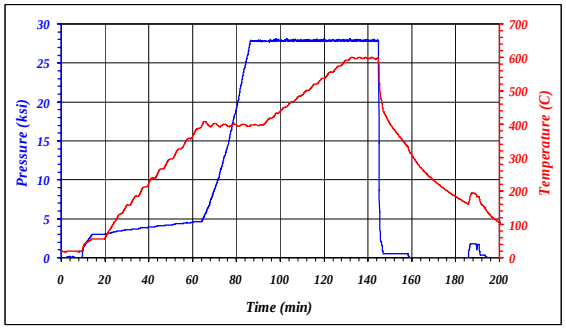

Figure 9. 0 vol. % - Pressure and temperature profile seen by can

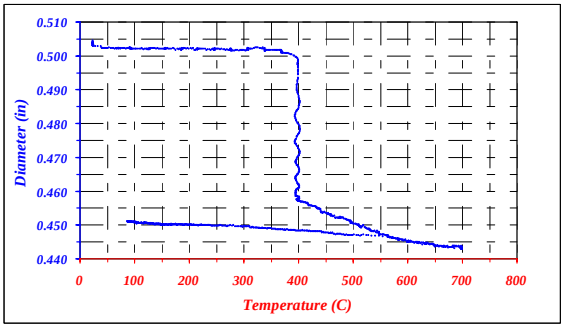

Figure 10. 10 vol. % - Outside can diameter shrinkage vs. temperature

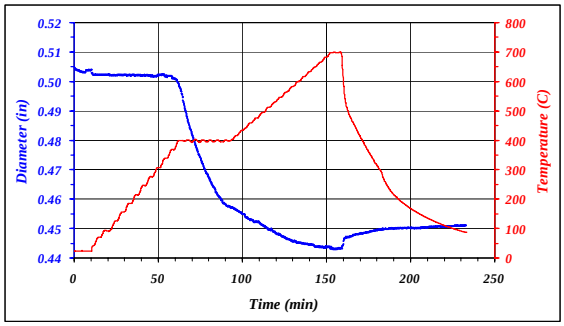

Figure 11. 10 vol. % - Outside can diameter shrinkage and temperature vs. time

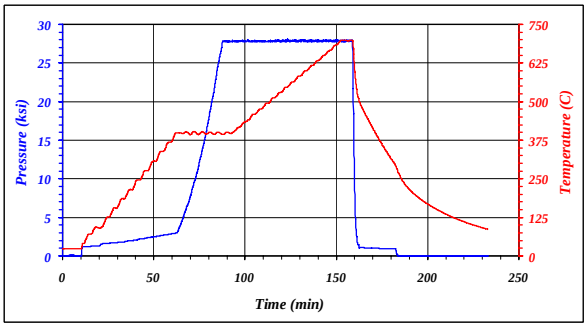

Figure 12. 10 vol. % - Pressure and temperature profile seen by can

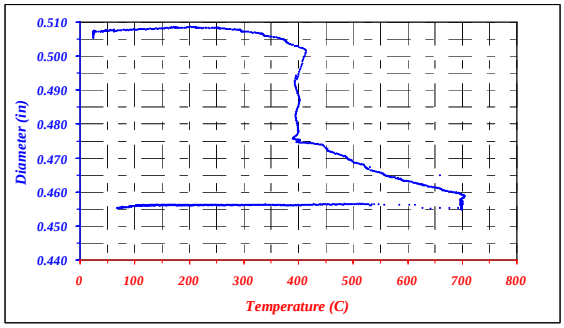

Figure 13. 25 vol. % - Outside can diameter shrinkage vs. temperature

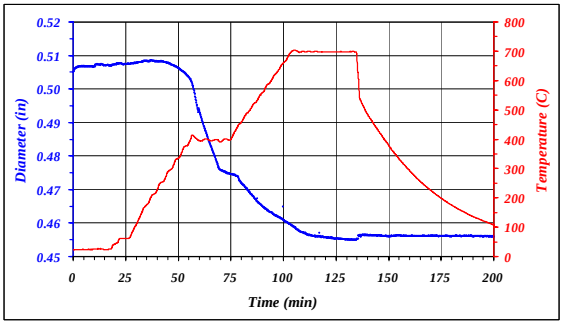

Figure 14. 25 vol. % - Outside can diameter shrinkage and temperature vs. time

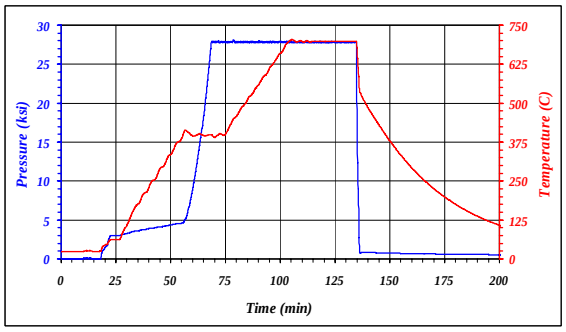

Figure 15. 25 vol. % - Pressure and temperature profile seen by can

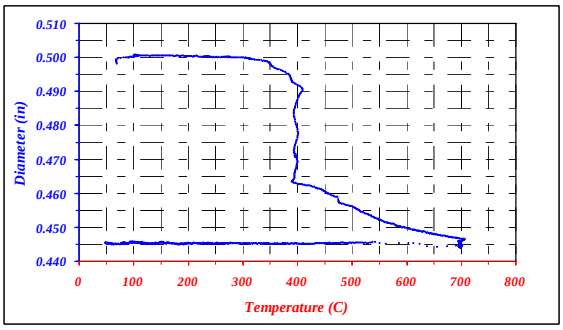

Figure 16. 45 vol. % - Outside can diameter shrinkage vs. temperature

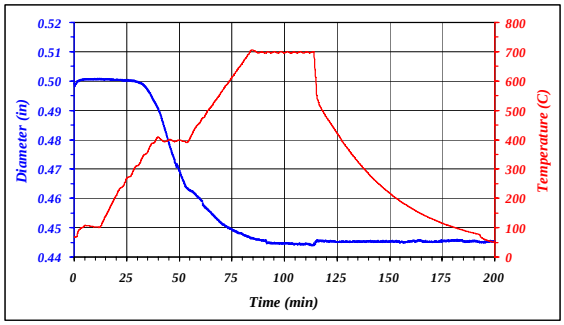

Figure 17. 45 vol. % - Outside can diameter shrinkage and temperature vs. time

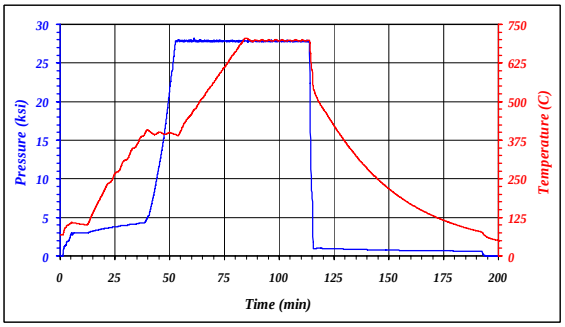

Figure 18. 45 vol. % - Pressure and temperature profile seen by can

3.4 Analysis of Composite Samples

The composite samples were analyzed using several apparatus. It was necessary to understand the degree of densification achieved as well as the resulting mechanical properties of the composites. Other questions of interest are the extent of reinforcement crystallization, the strength of the reinforcement/matrix interface, and the strengthening relation to reinforcement volume fraction. The cylindrical samples from the HIP were machined into various geometries for testing.

A Struers Accutom-5 with a diamond wheel cut discs approximately 1 mm in thickness for use in microscopy and hardness testing. The microscopy discs were polished to 0.05 μm, and were analyzed with an Olympus BH2 microscope combined with a Hitachi digital camera. A Leo 1550 Field Emission Scanning Electron Microscope (SEM) with an IXRF Microanalysis System used for Energy Dispersive Spectroscopy (EDS) was also used to examine the samples. The backscattering detector was employed for the majority of the SEM analysis because of its capability in distinguishing phases.

The hardness testing was performed on the microscopy samples after they had been analyzed. Vickers macro-hardness testing was conducted using a Leco V-100-A2 with a load of 10kg. Vickers micro-hardness testing was conducted using a Leco DM-400 with a load of 25g. The load was applied for 10 seconds.

A second set of discs were cut for XRD scans. Using the Accutom, they were sliced into a tetragonal shape with dimensions 3x3 mm and a 1 mm thickness. The samples were adhered to a glass slide using clear nail polish, and then mounted for scanning. Scans were run to measure the diffraction angle from 20-110º using Cu Kα radiation at a speed of 4º per minute.

After the discs were made, a CNC mill machine was used to cut each cylindrical sample into three smaller cylinders for compression testing. The mill was programmed to cut in a circular pattern around a 0.1-inch radius and was lowered in 0.025-inch increments. After .44 inches had been machined vertically, a hacksaw or the Accutom was used to remove the smaller cylinder from the rest of the sample. The ends of the cylinders were made parallel with less than a 0.001 inch tolerance using a file and calipers. The final length and diameter dimensions were ~10mm x 5mm, yielding a 2:1 aspect ratio. This ratio was chosen to avoid excessive buckling or "pancaking" during compression. Before these samples were deformed, they were measured for apparent density and closed porosity by two methods. The first was Archimedes' Principle on an Archimedes scale in ethanol where the dry and submerged weights were measured, and the second was placing them inside the helium pycnometer. Then the samples were tested in compression at the rate of 0.2 mm/min using an Instron 4468.

Post-compression microscopy of the deformed cylinder samples was done using SEM. The samples were cut in half using the Accutom, along the Z or length axis, such that the mounted face could have the compression axis aligned in the SEM in the vertical or Y dimension. The samples were prepared in the same manner as described earlier in this section.

Chapter Four – Experimental Results

4.1 Analysis of Reinforcement Powder Particles

4.1.1 X-ray Diffraction Results

Comparisons of the XRD patterns of un-milled NiW powder and milled reinforcement powder in Figure 19 confirmed that the 30 hour milled samples contained no crystalline nickel peaks and a broad halo at the Ni[111]. Crystalline tungsten peaks are broader but still visible in the milled reinforcement.

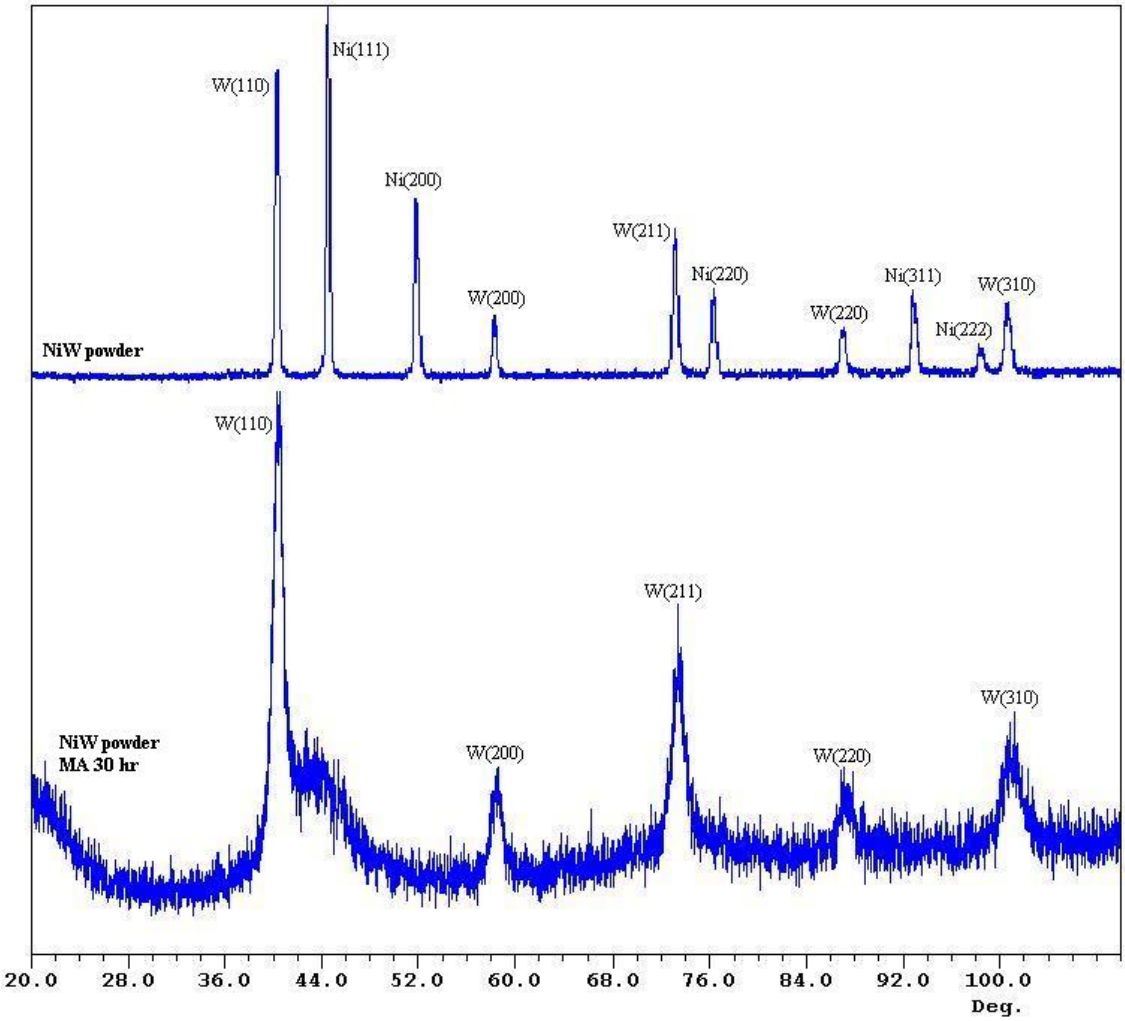

Figure 19. XRD patterns of un-milled and milled NiW

4.1.2 Particle Size

A median reinforcement particle diameter of 37.5 μm was measured by the Horiba particle size analyzer.

4.2 Analysis of Composite Samples

4.2.1 X-ray Diffraction Results

XRD patterns of the three composites are in Figure 20. The patterns display crystalline nickel peaks from the matrix as well as crystalline tungsten peaks from the reinforcement.

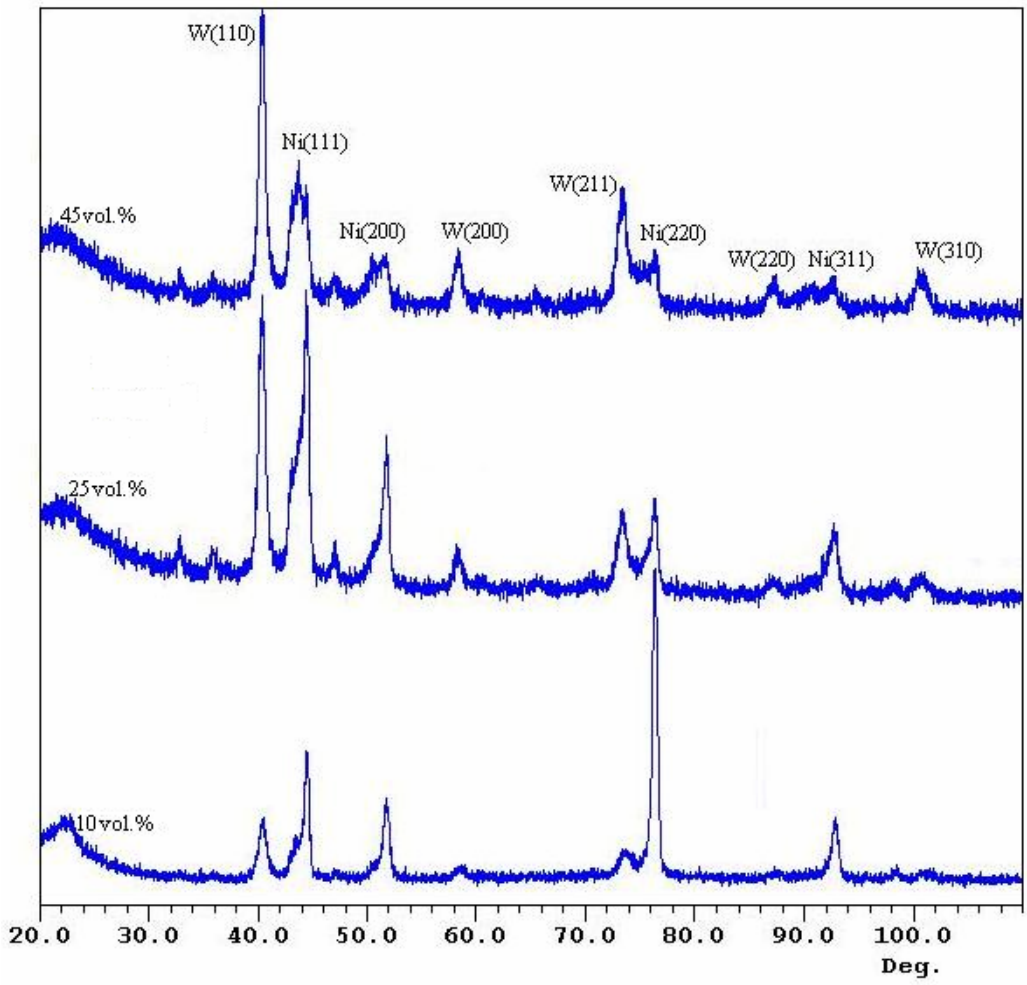

Figure 20. XRD patterns of 10, 25, and 45 vol. % reinforcement composites. Nickel peaks become shorter and broader with increasing reinforcement.

If the reinforcement contained fully crystalline nickel, then the nickel peaks shown would be very narrow and defined. The patterns however show broader nickel peaks; the higher the volume fraction of reinforcement the broader the peaks.

4.2.2 Microscopy

Optical micrograph examples are seen in Figures 21-24.

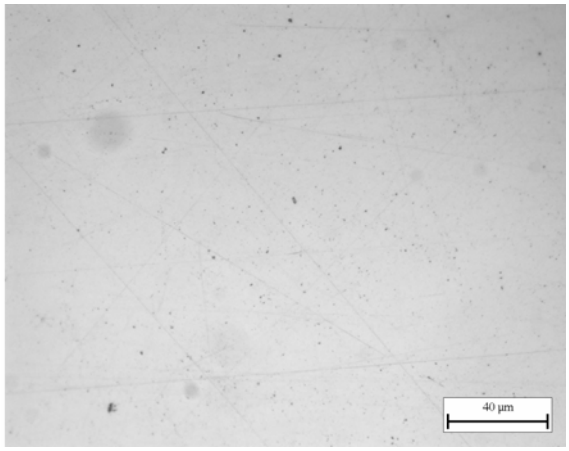

Figure 21. Optical micrograph of a 0 vol. % reinforcement sample – pure nickel

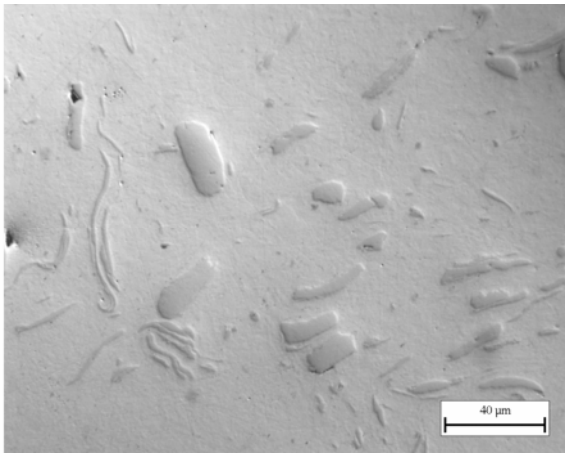

Figure 22. Optical micrograph of a 10 vol. % reinforcement composite

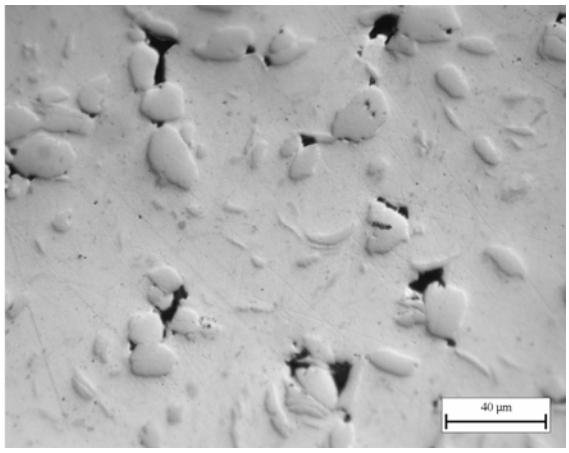

Figure 23. Optical micrograph of a 25 vol. % reinforcement composite

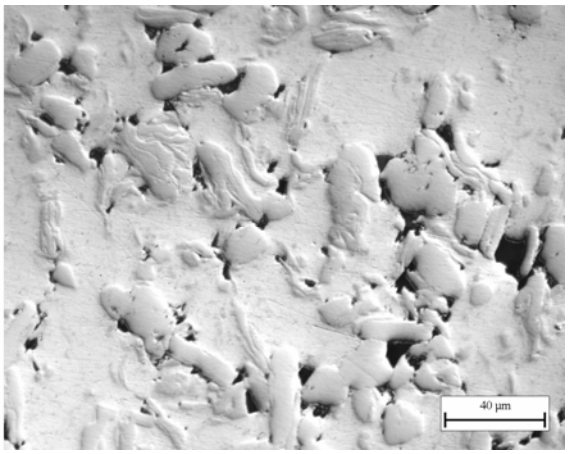

Figure 24. Optical micrograph of a 45 vol. % reinforcement composite

Porosity tends to be surrounded by particulates. Figure 25 is an SEM image of the highly dense 0 vol. % reinforcement sample. Figures 26-28 show good particulate dispersion in the reinforced composites.

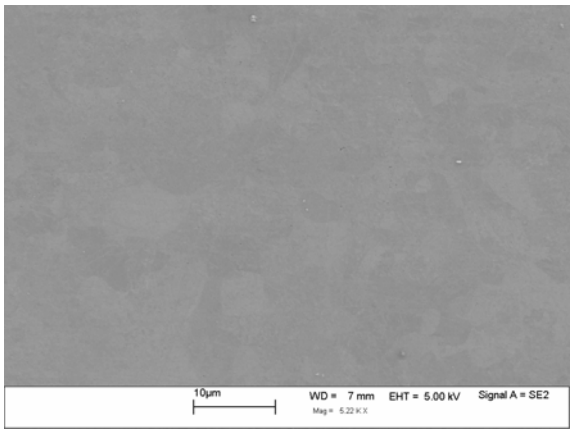

Figure 25. Highly dense pure nickel sample

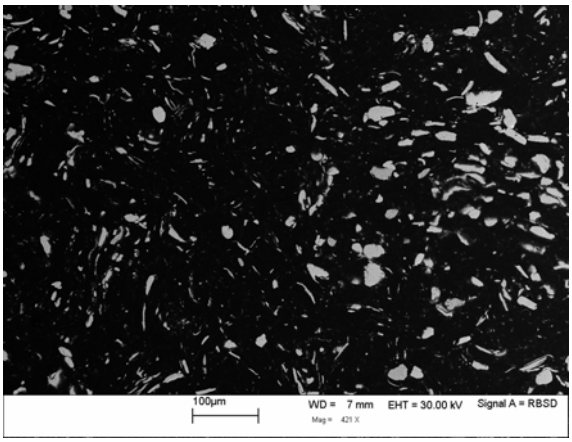

Figure 26. Random particulate dispersion in 10 vol. % reinforcement composite

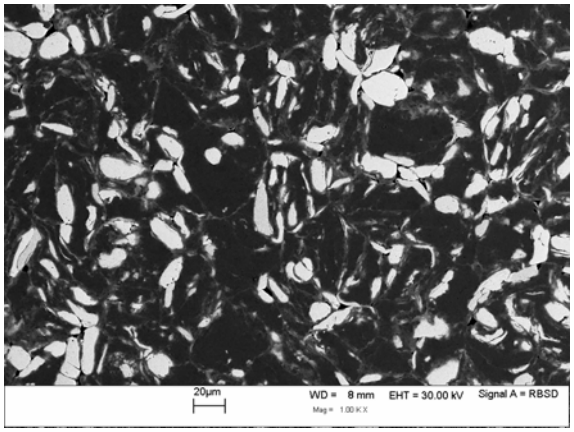

Figure 27. Random particulate dispersion in 25 vol. % reinforcement composite

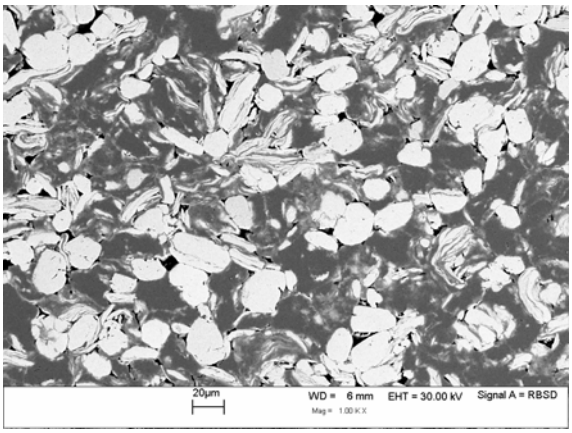

Figure 28. Random particulate dispersion in 45 vol. % reinforcement composite

EDS confirmed Ni and W within the reinforcement particulates. In addition, when the reinforcement particles were examined at a high magnification they show a two-phase structure with several small brighter spots indicative of a higher atomic number. Figure 29 and Figure 30 show these sub-particles within the reinforcement.

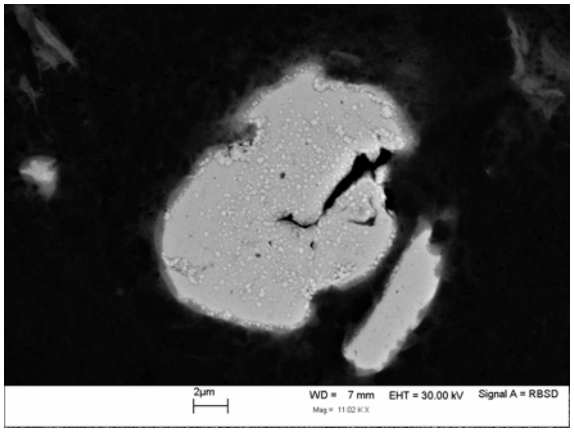

Figure 29. Sub-particles embedded in a reinforcement particle of a 10 vol. % reinforcement composite

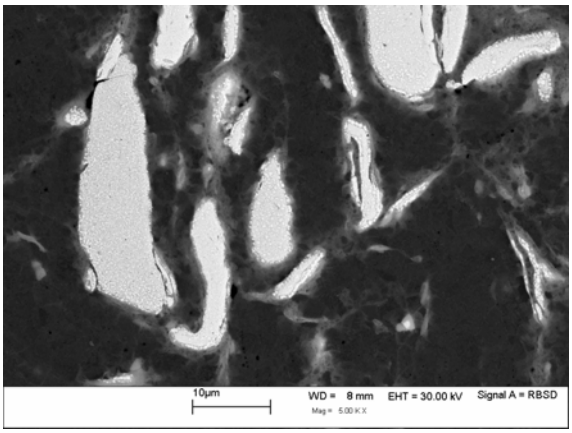

Figure 30. Sub-particles embedded in a reinforcement particle of a 25 vol. % reinforcement composite

4.2.3 Compression Tests

The stress-strain curves for the three cylinders of each HIP sample is shown in Figure 31:

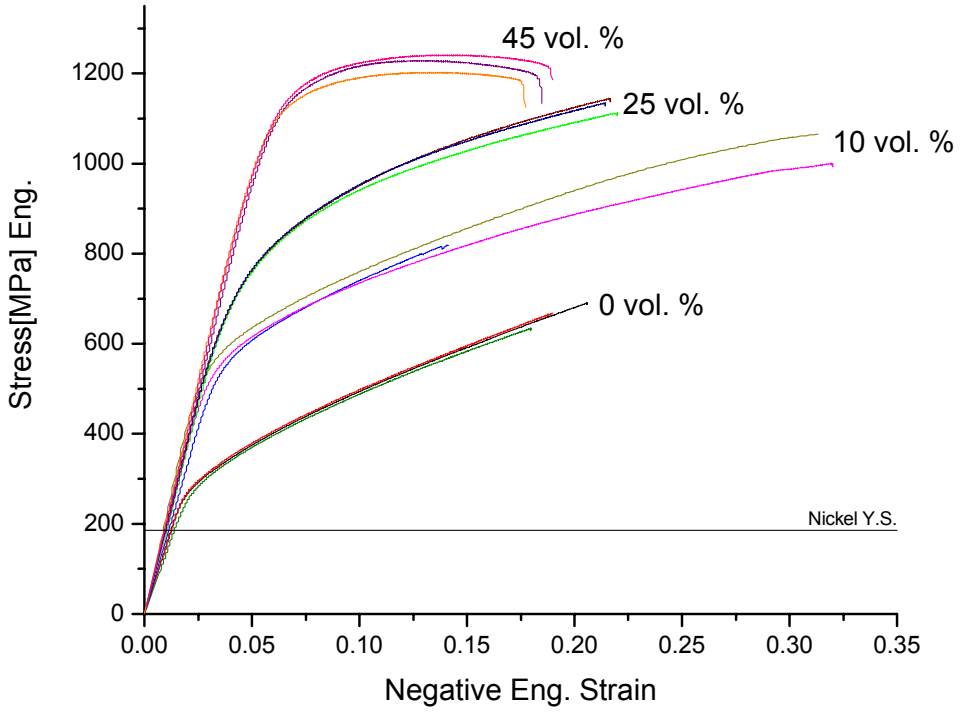

Figure 31. Compression test results for the three composites and the pure nickel compact

The yield stress of the samples was calculated using a 0.2% strain offset, and the raw data is tabulated in Appendix A. Figure 32 shows the increase in average yield stress with increasing reinforcement volume percent.

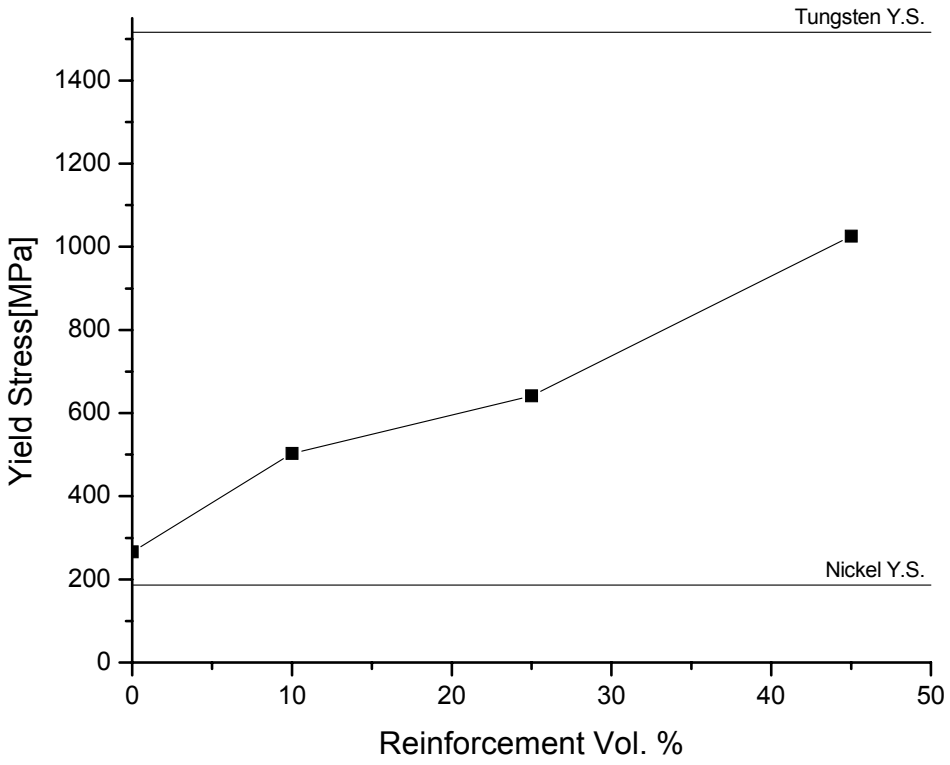

Figure 32. Plot of average yield stress vs. reinforcement volume percent

The Young's Modulus for the samples slightly increased for the high reinforcement volume fraction composites; however, a strain gauge was not used and thus not accurate. The strain value obtained was from the displacement of the compression plates during testing.

Post-compression SEM images of the composites show reinforcement particulate fractures in Figures 33-35. The 45 volume % reinforcement composite samples were the only samples to fracture during compression testing. A SEM micrograph of the fracture surface is shown in Figure 36.

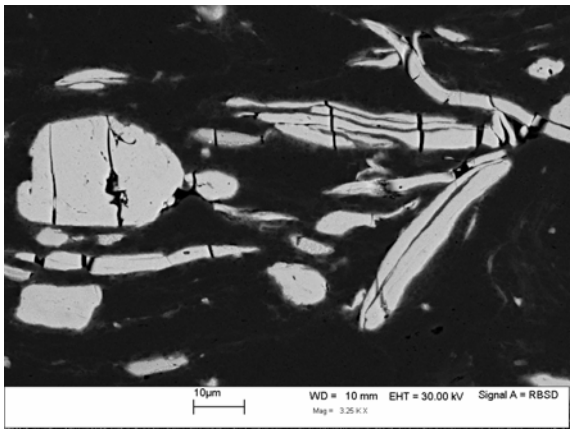

Figure 33. Particulate fractures in post-compression 10 vol. % reinforcement composite – aligned with compression in vertical axis

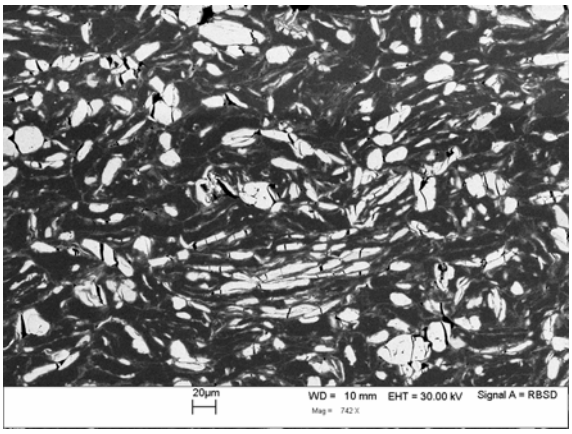

Figure 34. Particulate fractures in post-compression 25 vol. % reinforcement composite – aligned with compression in vertical axis

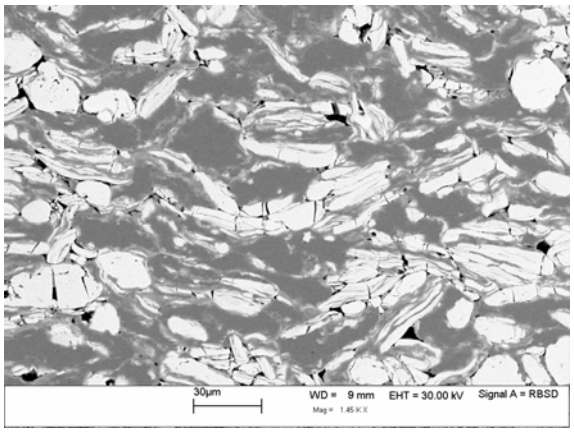

Figure 35. Particulate fractures in post-compression 45 vol. % reinforcement composite – aligned with compression in vertical axis

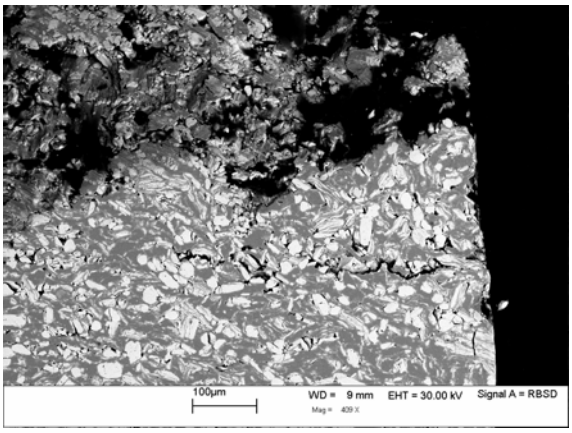

Figure 36. Angular view of fracture surface also showing second failure initiation in 45 vol. % reinforcement composite

4.2.4 Vickers Hardness Tests

The Vickers hardness test method consists of indenting the test material with a diamond indenter, in the form of a right pyramid with a square base and an angle of 136 degrees between opposite faces. The two diagonals of the indentation left in the surface of the material after removal of the load are measured using a microscope. Equation [5] shows the calculation for HV.

$$HV = \frac{2F\sin\left(\frac{136°}{2}\right)}{d^2} \approx 1.854\frac{F}{d^2} \quad [5]$$

Here, F is the load in kg and d is the diagonal measured in mm.

Vickers macro-hardness and micro-hardness tests were performed on the composite samples. For the composites macro-hardness, ten measurements were made for each composite (see table in Appendix B), and the standard deviation was about 3%. The averages of the results are shown in Table 2 below.

Table 2. Averages of Vickers macro-hardness measurements on composite samples

Vickers Macro Hardness - 10kg							
0 vol. %		10 vol. %		25 vol. %		45 vol. %	
µm	HV	µm	HV	µm	HV	µm	HV
377	**131**	300	**207**	267	**261**	229	**355**

Figure 37 shows the increase in average composite macro-hardness with increasing reinforcement volume fraction.

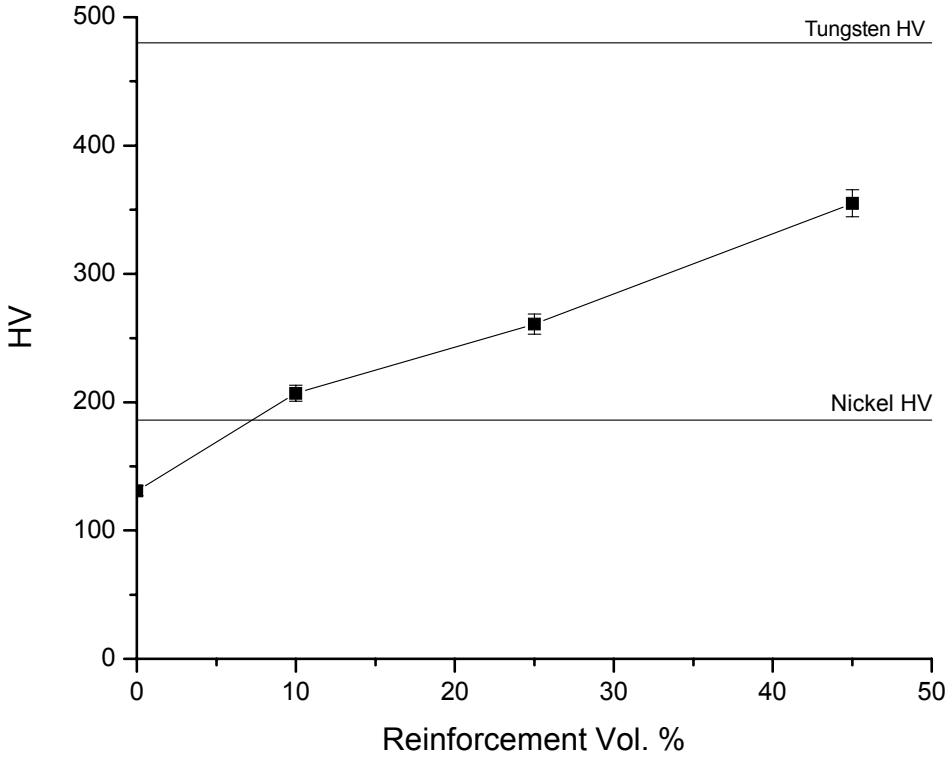

Figure 37. Plot showing average composite Vickers macro-hardness increase with higher volume fraction of reinforcement

With the Vickers micro-hardness testing, several measurements were made for the matrix and the reinforcement particles in the differing composites. The matrix hardness was consistent among the composites and averaged 118 HV with a standard deviation of 6%. The resulting particle HV in the composite samples varied greatly due to difficulty in hitting a particle and the size of the particle. The data was too widespread to make any conclusions about particle hardness in any of the samples. The highest value recorded was 766 HV, with several numbers in the 500-700 HV range.

4.2.5 Density and Porosity Calculations

Density calculations were conducted to measure the porosity of the composites after consolidation. Theoretical density was calculated using the rule of mixtures (ROM) as shown in Equation [6].

$$\rho_{theoretical} = \rho_{matrix} V_{matrix} + \rho_{reinforcement} V_{reinforcement} \quad [6]$$

Here, V_{matrix} and $V_{reinforcement}$ are the volume fractions of the matrix and reinforcement, while ρ_{matrix} and $\rho_{reinforcement}$ are the densities. Porosity of the composites was measured by two means: the Archimedes' Principle and a helium pycnometer. The Archimedes' Principle can be used to determine the volume and therefore the density of an object by measuring its buoyant force when submerged in a liquid. The apparent density (ρ_{app}), which is the density of the material including its closed pores, can be calculated by Equation [7].

$$\rho_{app} = \frac{W_{dry}\rho_{liquid}}{W_{dry} - W_{submerged}} \quad [7]$$

Ethanol was used as the liquid because of its superior wetting capability compared to water. After the dry weight (W_{dry}) and submerged weight ($W_{submerged}$) were measured on an Archimedes scale, the composites apparent density was calculated using Equation [7]. With the theoretical and apparent densities calculated, Equation [8] is used to find the % closed porosity.

$$\left[1 - \frac{\rho_{app}}{\rho_{theoretical}}\right] 100 = \% \text{ closed porosity} \quad [8]$$

The helium pycnometer was also utilized to measure the apparent density of the composite samples, and the same Equation [8] above was applied to calculate the closed porosity. Image analysis was additionally used to determine porosity. ImageJ, the software used, is described in more detail in Section 5.4. The brightness of the optical micrographs was adjusted such that the particles and matrix were close to white, and the remaining black pixels indicated closed porosity. Using ImageJ, the function Binary/Threshold changed the image from greyscale to black/white. The particles and matrix were made into white particles, and the porosity was left as black pixels. The Analyze/Histogram operation counted the number of black pixels, white pixels, and total pixels. Dividing the total pixel count of the micrograph by the black pixels yielded an estimated % closed porosity [50]. The results of the three different measurements of apparent density and corresponding closed porosity calculations are shown in Figure 38 and Table 3.

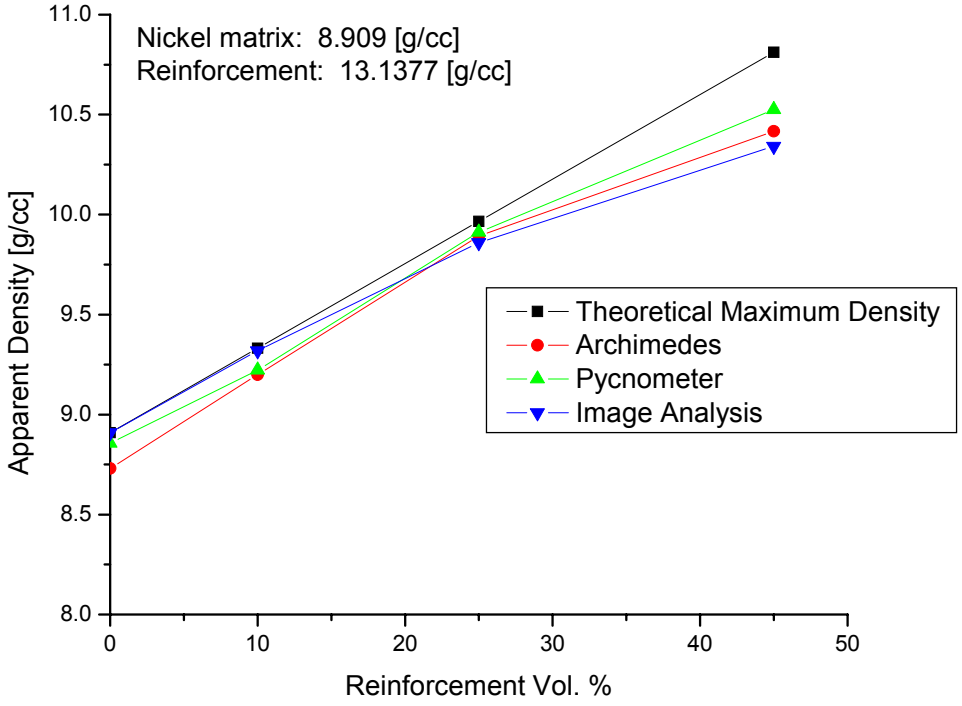

Figure 38. Apparent density measurements for composite samples using three different techniques

Table 3. Density and porosity values calculated using different analysis techniques

Reinforcement Vol. %	Theoretical ρ[g/cc]	% Closed Porosity		
		Archimedes	Pycnometer	Image Analysis
0	8.909	2.003	0.578	0.000
10	9.332	1.417	1.180	0.145
25	9.966	0.744	0.544	1.062
45	10.812	3.655	2.661	4.349

Chapter Five – Discussion

A general trend seen from the experimental results in Chapter Four is the increase in strength, hardness, and porosity with increasing volume fraction of reinforcement. In order to fit the strength and hardness trends to a model it is necessary to define strengthening mechanisms in composites which have discontinuous non-aligned reinforcement in a ductile matrix. Three mechanisms will be considered here: work hardening due to mismatch of the coefficient of thermal expansion (ΔCTE), Orowan strengthening, and boundary strengthening.

5.1 ΔCTE strengthening

One strengthening factor in discontinuous particulate reinforced composites is work hardening caused by mismatch of the coefficient of thermal expansion, or ΔCTE [4]. During cooldown from processing, residual stresses develop near the particles due to the mismatch. The misfit strain is approximated in Equation [9].

$$\varepsilon_{\Delta CTE} = \frac{\Delta CTE \bullet \Delta T}{2} \qquad [9]$$

Here, ΔCTE is the difference in coefficients of thermal expansion between the matrix and reinforcement, ΔT is the temperature difference from processing to ambient temperature, and $\varepsilon_{\Delta CTE}$ is the misfit strain. If the associated misfit stress is higher than the yield stress of the matrix, dislocations are created near the interface to relieve the stress. The ΔCTE generated dislocation density will be

$$\rho_{\Delta CTE} = \frac{2 f \varepsilon_{\Delta CTE}}{b(1-f)} \bullet \left(\frac{s}{v}\right) \qquad [10]$$

where f is the volume fraction of reinforcement, b is the magnitude of the matrix Burger's vector, and (s/v) is the surface to volume ratio of the reinforcement. From strengthening theory due to work hardening we have

$$\sigma_c = \sigma_0 + \alpha' G b \sqrt{\rho_{\Delta CTE}} \quad [11]$$

where α′ is a fitting parameter with a value approximately equal to one, *G* is the elastic shear modulus of the matrix, σ_c is the flow stress of the composite, and σ_0 is the associated flow stress of the matrix. From Equations [9-11] above, a large CTE mismatch will result in a high misfit strain, dislocation density, and hardening contribution [4]. Combining these three equations yields the ΔCTE strengthening contribution in Equation 12.

$$\Delta\sigma_{\Delta CTE} = \alpha' G \sqrt{\left(\frac{f \bullet \Delta CTE \bullet \Delta T}{1 - f} \bullet b \bullet \frac{s}{v} \right)} \quad [12]$$

The CTE values for Ni and W are shown in Table 4.

Table 4. Thermal expansion values for nickel and tungsten [51]

Metal	CTE (μm/m°C) Temp. 27°C
Ni	13.3
W	4.6

The composites were cooled to and tested at ambient temperature; therefore the CTE values at 27°C were used to predict the ΔCTE strengthening. The ΔT for each composite was calculated as the difference from the maximum temperature reached in the HIP profile to ambient temperature.

The amorphous reinforcement CTE would be between the nickel and tungsten values. Four commonly used models to predict the CTE of MMCs are Turner, Kerner, ROM, and Schapery [52-55]. The Turner model was used to estimate the CTE of the reinforcement. It assumes a homogeneous strain throughout the material and a balance of the internal average stresses to derive the expansivity of a two-component composite as follows

$$\alpha_{mmc} = \frac{\alpha_p V_p K_p + \alpha_m V_m K_m}{V_p K_p + V_m K_m} \quad [13]$$

where K is the bulk modulus, V is the volume fraction, and α is the CTE. The subscripts *mmc*, *p*, and *m*, denote composite, particle, and matrix respectively. For the NiW reinforcement, tungsten and nickel material properties were used in Equation [13] in substitution of particle and matrix properties, respectively. The estimated NiW reinforcement CTE is 7.09 x 10^{-6}/°C.

5.2 Orowan strengthening

Orowan strengthening is defined as resulting from the resistance of dislocation line motion "through" a reinforcement particulate, and is seen in dispersion strengthened MMCs. Dislocation lines travel on closed packed planes in closed packed directions, and small reinforcement particulates will hinder the dislocation motion by absorbing energy through the formation of Orowan loops thus causing strengthening [27] as illustrated in Figure 39.

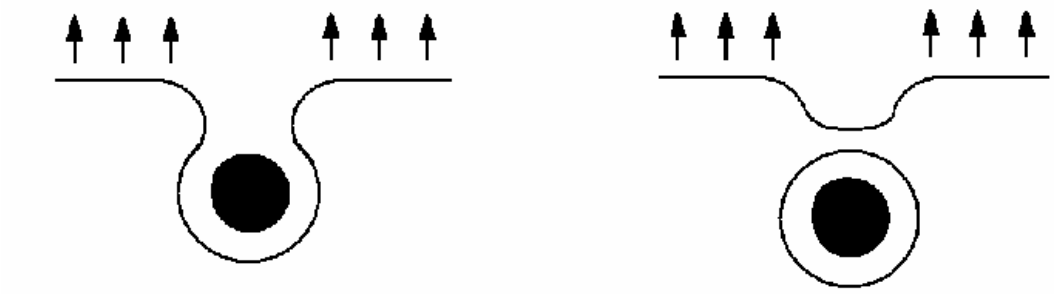

Figure 39. Orowan process of a dislocation bowing around a particle and leaving a dislocation loop

The strengthening predicted by the Orowan equation, $\sigma_{c,ds}$, is given by

$$\sigma_{c,ds} \cong \sigma_0 + \frac{3Gb}{L_{e-e}} \qquad [14]$$

where the interparticle spacing variable, $L_{e\text{-}e}$, is the edge-to-edge reinforcement spacing, G is the elastic shear modulus of the matrix, b is the magnitude of the matrix Burger's vector, $\sigma_{c,ds}$ is the flow stress of the composite, and σ_0 is the associated flow stress of the matrix. Equation [14] predicts $\sigma_{c,ds}$ reaches ∞ as $L_{e\text{-}e}$ approaches zero. The Ashby-Orowan equation is a modification to the Orowan equation which takes into account a minimum reinforcement size of an atomic

diameter. If the reinforcement size is too small, it becomes a solute atom and loses its ability to provide strengthening by interacting with dislocations in an incoherent manner. The dislocation core radius, r_0, is the scaling term in Equation [15] which identifies when strengthening by Orowan loops no longer exists for a particle of size d_r. The dislocation core radius in the Ashby-Orowan equation is physically the size of the dilated lattice under a dislocation, where a solute atom could be located. The strengthening contribution as predicted by the Ashby-Orowan equation for polycrystalline particle-hardened systems is

$$\Delta\sigma = \frac{2.4Gb}{2\pi(1-\nu)^{0.5}} \bullet \frac{\ln(d_r / r_0)}{L_{e-e}} \qquad [15]$$

where d_r is the reinforcement diameter, r_0 is the dislocation core radius, and v is the Poisson's ratio of the matrix [27].

5.3 Boundary strengthening

For coarse or widely spaced particles, the Orowan equation will not predict observed values of strengthening, as strengthening will be a function of L_{e-e}. Composite strengthening can be explained by the presence of particle/matrix boundaries and the associated constraints these have on dislocation motion [56]. In metals, as the matrix deforms dislocations will accumulate near boundaries and exert a shear stress on the boundaries. The increased dislocation density thus results in hardening or strengthening in the adjacent matrix, in a way that is mechanistically similar to the Hall-Petch effect. The predicted boundary strengthening is

$$\sigma_{c,B} = \sigma_0 + \sqrt{\frac{\tau_{boundary} \bullet Gb}{L_{e-e}}} = \sigma_0 + k\sqrt{\frac{1}{L_{e-e}}} \qquad [16]$$

where $\sigma_{c,B}$ is the composite flow stress, σ_0 is the associated matrix flow stress, $\tau_{boundary}$ is the shear stress at the matrix/reinforcement (M/R) boundary, G is the elastic shear modulus of the matrix, b is the magnitude of the matrix Burger's vector, and L_{e-e} is the reinforcement interparticle spacing [56].

Depending on the matrix, reinforcement, and M/R boundary shear stress properties, there are four boundary strengthening equation models. These shear stress properties are denoted by τ_{matrix}, $\tau_{reinforcement}$, and $\tau_{boundary}$ respectively. Which of the four models used depends on the behavior of the composites, so the composites are often experimentally tested beforehand. If the reinforcement particles have fractured, then $\tau_{boundary} > \tau_{reinforcement\text{-}fracture}$, and the boundary strengthening contribution can be predicted as

$$\Delta\sigma = \alpha' \sqrt{\frac{G_m \bullet G_p \bullet b}{5L_{e-e}}} \qquad [17]$$

where G_m is the shear modulus of the matrix, G_p is the shear modulus of the particle, b is the magnitude of the matrix Burger's vector, $L_{e\text{-}e}$ is the interparticle spacing, and α' is a fitting factor approximately equal to one [56]. If the composite shows matrix deformation or fracture, then $\tau_{reinforcement\text{-}fracture} > \tau_{boundary} > \tau_{matrix\text{-}fracture}$, and the boundary strengthening contribution can be predicted as Equation [18].

$$\Delta\sigma = \alpha'' \sqrt{\frac{G_m^{\,2} \bullet b}{5L_{e-e}}} \qquad [18]$$

Here, α″ is a fitting parameter approximately equal to one [56]. The other two boundary equations will not be included in this discussion because the modeled behavior does not match the compression results in Section 4.2.3. Particulate fractures are seen in the post-compression micrographs in Section 4.2.3, but the matrix had also yielded due to loading beyond the composite yield stress. It is not clear whether the particulates or the matrix yielded first, thus Equation [18] will be used to estimate boundary strengthening because it is more conservative than Equation [17]. To fit the Ashby-Orowan or boundary strengthening equations to the compression data, $L_{e\text{-}e}$ needs to be estimated.

5.4 $L_{e\text{-}e}$ estimation using image analysis

$L_{e\text{-}e}$ can be estimated by using the line-intercept method [57] to obtain average center-to-center spacings, and then subtracting twice the reinforcement particle radius. ImageJ is a public domain Java image processing program inspired by NIH Image, which can edit, analyze, and process optical or SEM micrographs [50]. Using the procedure outlined in Appendix C, ImageJ in conjunction with Mathematica was used to estimate the average $L_{e\text{-}e}$ of each composite sample. A copy of the program written for Mathematica is in Appendix D. Appendix E shows the average reinforcement interparticle spacing values calculated for each SEM micrograph. There is no reinforcement $L_{e\text{-}e}$ for the pure nickel sample. The distance between the grain boundaries in the pure nickel sample is approximately the average diameter of the particles, which is ~40 μm for -325 mesh nickel. Table 5 below shows the Mathematica program calculated results for the different composite samples, and also includes the grain boundary spacing for the pure nickel sample.

Table 5. Average calculated reinforcement particle spacing

Reinforcement Vol. %	Average $L_{e\text{-}e}$ [μm]	$L_{e\text{-}e}$ Standard Deviation
0	*40*	
10	28.54	11.36
25	11.93	4.17
45	6.29	1.99

5.5 Calculated Strengthening contributions

To calculate the strengthening contributions based on the models above, several assumptions have to be made. The shape of the reinforcement particles was assumed to be an oblate spheroid shape for *(s/v)* in Equation [12]. From solute atom lattice distortion measurements in nickel [58], r_0 was estimated to be one and a half times the Burger's vector in Equation [15]. The $L_{e\text{-}e}$ data was used in the Ashby-Orowan and boundary strengthening estimations. Figure 40 shows the three different strengthening contributions to the MMC strength and the experimental strengthening value.

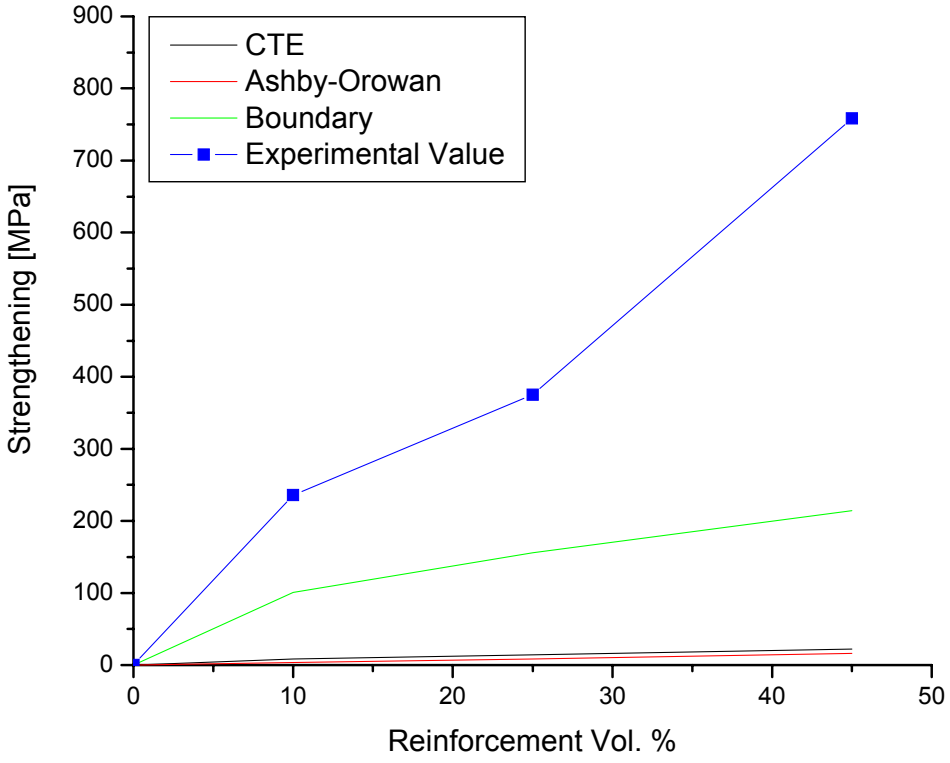

Figure 40. Calculated strengthening contributions to MMCs

As shown in Figure 41, the strengthening seen in the composite samples was greater than the sums of the ΔCTE, Ashby-Orowan, and boundary contributions. This extra strengthening could have been gained from other factors such as shear-load transfer, solid-solution strengthening, or grain size refinement. Shear-load transfer is indicated by the particle cracking in the post-compression SEM images. Solid-solution could have occurred during blending of the powders in the attritor. Some tungsten from the reinforcement powder could have diffused into the nickel matrix. Also during blending the nickel powder grain size could have been reduced and added a Hall-Petch strengthening effect. Even though there exists secondary strengthening from other factors, the conservative boundary strengthening calculation is likely the source of the experimental and model discrepancy. If the shear modulus of the reinforcement particulates was measured, and it was observed that particle cracking initiated before matrix deformation, Equation [17] could be accurately used to calculate a higher boundary strengthening contribution.

Boundary strengthening is the most dominant of the three calculated models in spite of the conservative calculation. Boundary strengthening has a relationship proportional to the inverse square root of $L_{e\text{-}e}$. Figure 41 and Figure 42 show yield strength and hardness versus the inverse square root of $L_{e\text{-}e}$, respectively.

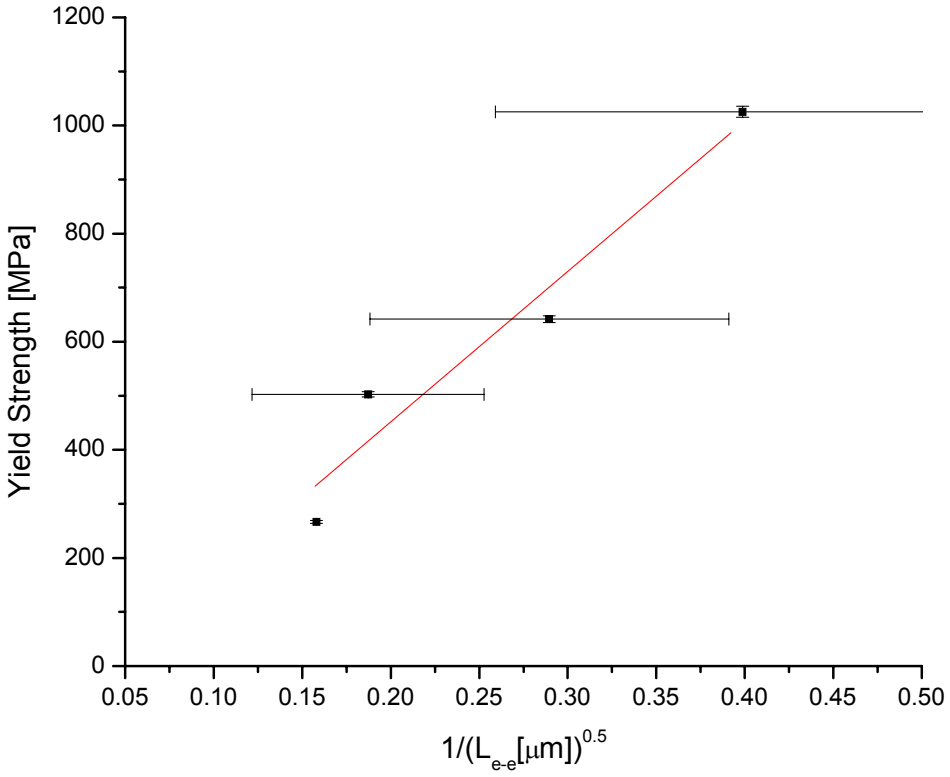

Figure 41. Plot of yield strength versus inverse square root of reinforcement particle spacing

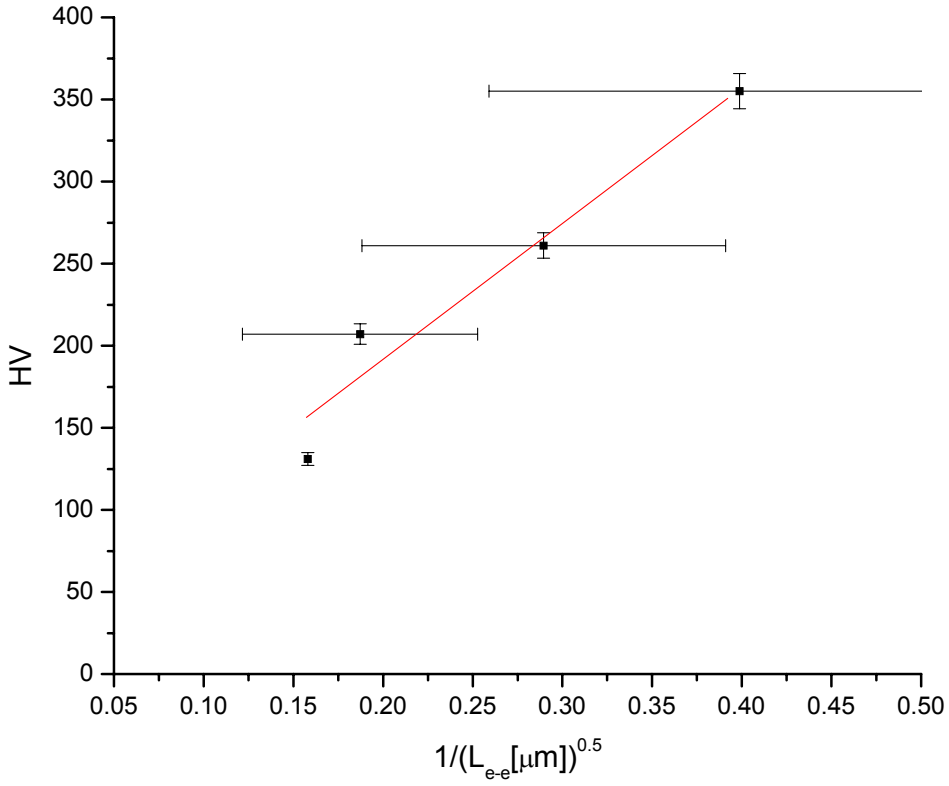

Figure 42. Plot of Vickers macro-hardness versus inverse square root of reinforcement particle spacing

The large error bars of the spacing data in Figure 41 and Figure 42 are one standard deviation. The spacing value estimated in Section 5.4 was averaged from each line drawn on each micrograph which each represented an average of several $L_{e\text{-}e}$ distances, and is listed in Appendix E. The averages of the $L_{e\text{-}e}$ values per line vary, but the final average $L_{e\text{-}e}$ value for each composite as seen in Table 5 is a mean of a couple hundred $L_{e\text{-}e}$ values and likely an accurate estimation. The data shows an increasing trend which fits well to a $1/L_{e\text{-}e}^{0.5}$. The increasing trends versus reinforcement particle spacing in Figure 41 and Figure 42 are similar. Figure 43 is a plot of the yield strength versus the Vickers macro-hardness.

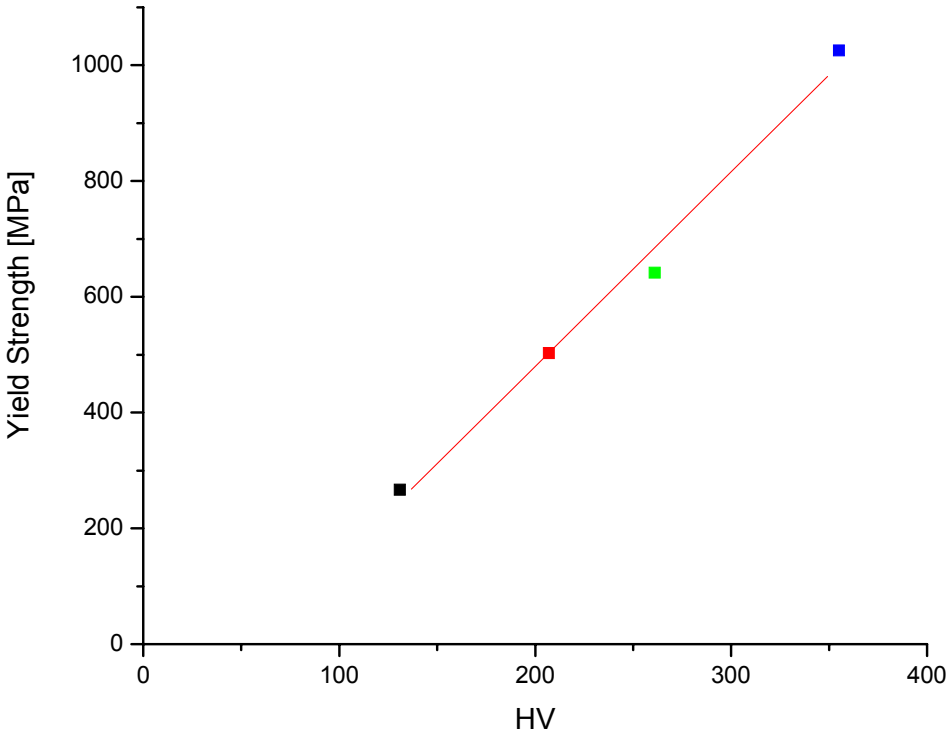

Figure 43. Plot of yield strength versus Vickers macro-hardness for the pure nickel sample and the three composites

Chapter Six – Conclusions

Reinforcement particles showing no nickel crystalline peaks in XRD patterns were produced using MA. SEM/EDS on the NiW reinforcement showed no signs of significant oxidation or iron/chromium contamination from the grinding media. The HIP consolidation was successful in making a high density compact from metal powder. The mechanical strength of the particulate reinforced MMCs was significantly higher than pure nickel, with an increase of 284% yield strength and 171% HV between the pure nickel samples and the 45 vol. % reinforcement MMC. Strengthening model contribution calculations for discontinuously reinforced MMCs confirm boundary strengthening as the primary source of improved composite performance. The reinforcement/matrix interface was sufficiently strong for shear load transfer to occur, as indicated by the reinforcement cracking observed in the SEM micrographs of the deformed samples in Figures 33-35 [59].

Chapter Seven – Future Work

Continuing analysis of these composites would be beneficial. Using techniques such as Mossbaüer Spectroscopy, DTA, DSC, or TEM could confirm the extent of amorphization in the milled reinforcement as well as the reinforcement in the MMCs. XPS, AES, and EXAFS could examine the reinforcement/matrix interfacial bond.

Compression failure followed after the fracture of the reinforcement particulates. With this stalwart particle/matrix interface, the ensuing research may include maximizing the matrix strength. Reduction of porosity during the HIP consolidation would also help in composite strengthening. It is possible to use smaller sized nickel powder to achieve greater packing density.

References

1. Dicarlo, J.A. *Fibers for Structurally Reliable Metal and Ceramic Composites.* Journal of Metals, 1985. **37**(6): p. 44-49.
2. Chawla, K.K. *Composite materials : science and engineering*. New York: Springer-Verlag, 1987.
3. Clyne, T.W. *An introduction to metal matrix composites*, ed. P.J. Withers. New York: Cambridge University Press, 1993.
4. Taya, M. *Metal matrix composites : thermomechanical behavior*, ed. R.J. Arsenault. Oxford, England; New York: Pergamon Press, 1989.
5. Schwarz, R.B. and P. Nash. *Using Amorphous Phases in the Design of Structural Alloys.* Jom-Journal of the Minerals Metals & Materials Society, 1989. **41**(1): p. 27-31.
6. Luborsky, F.E. *Amorphous Metallic Alloys*. London: Butterworths Monographs in Materials, 1983.
7. Klement, W., R.H. Willens, and P. Duwez. *Non-Crystalline Structure in Solidified Gold-Silicon Alloys.* Nature, 1960. **187**: p. 869-870.
8. Cheng, Y.T., W.L. Johnson, and M.A. Nicolet. *Studies on the Rules for Amorphous Phase Formation by Ion-Mixing in Metallic Systems.* Proceedings of the Society of Photo-Optical Instrumentation Engineers, 1985. **530**: p. 134-137.
9. Brimhall, J.L., H.E. Kissinger, and L.A. Charlot. *Amorphous Phase Formation in Irradiated Intermetallic Compounds.* Radiation Effects and Defects in Solids, 1983. **77**(3-4): p. 237-293.
10. Schwarz, R.B. and W.L. Johnson. *Formation of an Amorphous Alloy by Solid-State Reaction of the Pure Polycrystalline Metals.* Physical Review Letters, 1983. **51**(5): p. 415-418.
11. Koch, C.C., et al. *Preparation of Amorphous Ni60nb40 by Mechanical Alloying.* Applied Physics Letters, 1983. **43**(11): p. 1017-1019.
12. Quan, M.X., et al. *Solid-State Amorphization Transformations Induced by Mechanical Alloying.* Journal of Alloys and Compounds, 1993. **194**(2): p. 325-330.
13. Schwarz, R.B. and C.C. Koch. *Formation of Amorphous-Alloys by the Mechanical Alloying of Crystalline Powders of Pure Metals and Powders of Intermetallics.* Applied Physics Letters, 1986. **49**(3): p. 146-148.
14. Weeber, A.W. and H. Bakker. *Amorphization by Ball Milling - a Review.* Physica B, 1988. **153**(1-3): p. 93-135.
15. Lee, P.Y., et al. *Consolidation of amorphous Ni-Zr-Ti-Si powders by vacuum hot-pressing method.* Intermetallics, 2002. **10**(11-12): p. 1277-1282.
16. Mi, S. and T.H. Courtney. *Processing, structure and properties of Ni-W alloys fabricated by mechanical alloying and hot-isostatic pressing.* Scripta Materialia, 1998. **38**(4): p. 637-644.
17. Kim, H.J., et al. *Cu-based bulk amorphous alloys prepared by consolidation of amorphous powders in the supercooled liquid region.* Intermetallics, 2004. **12**(10-11): p. 1109-1113.
18. Lee, M.H., et al. *Synthesis of Ni-based bulk amorphous alloys by warm extrusion of amorphous powders.* Journal of Non-Crystalline Solids, 2003. **315**(1-2): p. 89-96.
19. Huang, X.S. and T. Mashimo. *Metastable BCC and FCC alloy bulk bodies in Fe-Cu system prepared by mechanical alloying and shock compression.* Journal of Alloys and Compounds, 1999. **288**(1-2): p. 299-305.
20. Huang, X.S. and T. Mashimo. *Preparation of Fe-W system metastable alloy bulk body by mechanical alloying and shock compression.* Journal of Materials Processing Technology, 1999. **85**(1-3): p. 135-137.
21. Huang, X.S. and T. Mashimo. *Metastable alloy bulk bodies in the Fe-W system prepared by mechanical alloying and shock compression.* Journal of Alloys and Compounds, 2000. **296**(1-2): p. 183-190.
22. Mashimo, T., S. Ozaki, and K. Nagayama. *Keyed-Powder Gun for the Oblique-Impact Shock Study of Solids in Several 10-S of Gpa Region.* Review of Scientific Instruments, 1984. **55**(2): p. 226-230.
23. Ye, L.L., et al. *Consolidation of MA amorphous NiTi powders by spark plasma sintering.* Materials Science and Engineering a-Structural Materials Properties Microstructure and Processing, 1998. **241**(1-2): p. 290-293.
24. De la Torre, S.D., et al. *Nickel-molybdenum catalysts fabricated by mechanical alloying and spark plasma sintering.* Materials Science and Engineering a-Structural Materials Properties Microstructure and Processing, 2000. **276**(1-2): p. 226-235.

25. Kawamura, Y., H. Mano, and A. Inoue. *Nanocrystalline aluminum bulk alloys with a high strength of 1420 MPa produced by the consolidation of amorphous powders.* Scripta Materialia, 2001. **44**(8-9): p. 1599-1604.
26. *Discussions with Dr. S. L. Kampe.*
27. Martin, J.W. *Micromechanisms in particle-hardened alloys*. Cambridge: Cambridge University Press, 1980.
28. Erich, D.L. *Metal-Matrix Composites - Problems, Applications, and Potential in the P/M Industry.* International Journal of Powder Metallurgy, 1987. **23**(1): p. 45-54.
29. Broutman, L.J. *Modern composite materials*, ed. R.H. Krock. Reading, Mass.: Addison-Wesley Pub. Co., 1967.
30. *Metal matrix composites. Processing and interfaces*, ed. R.K. Everett and R.J. Arsenault. Boston: Academic Press, 1991.
31. Hull, D. *An introduction to composite materials*. 2nd ed, ed. T.W. Clyne. Cambridge [England]; New York: Cambridge University Press, 1996.
32. Metcalfe, A.G. *Interfaces in metal matrix composites*. New York: Academic Press, 1974.
33. Piggott, M.R. *Load-bearing fibre composites*. Oxford; New York: Pergamon Press, 1980.
34. *Adhesion and bonding in composites*, ed. R. Yosomiya. New York: M. Dekker, 1990.
35. Benjamin, J.S. *Mechanical Alloying.* Scientific American, 1976. **234**(5): p. 40-49.
36. Sundaresan, R. and F.H. Froes. *Mechanical Alloying.* Journal of Metals, 1987. **39**(8): p. 22-27.
37. Spaepen, F. and D. Turnbull. *Rapidly Quenched Metals*, ed. N.J. Grant and B.C. Giessen. Vol. II. Boston: Cambridge, p. 205, 1976.
38. Johnson, W.L. *Thermodynamic and Kinetic Aspects of the Crystal to Glass Transformation in Metallic Materials.* Progress in Materials Science, 1986. **30**(2): p. 81-134.
39. Miedema, A. *Theory of Alloy Phase Formation*, ed. L. Bennett. New Orleans: AIME, 344, 1980.
40. Weeber, A.W. *Application of the Miedema model to formation enthalpies and crystallisation temperatures of amorphous alloys.* Journal of Physics F: Metal Physics, 1987. **17**(4): p. 809.
41. Shen, T.D., et al. *Amorphous Phase Formation in the Fe-W System Induced by Mechanical Alloying.* Mat. Sci. Forum, 1992. **88-90**: p. 391-398.
42. Shen, T.D., et al. *Amorphous Phase-Transition Mechanism by the Mechanical Alloying of the Fe-W System.* Journal of Applied Physics, 1992. **71**(4): p. 1967-1971.
43. Herr, U. and K. Samwer. *Formation of Nanocrystalline and Amorphous Phases by Mechanical Alloying in the System W-Fe.* Nanostructured Materials, 1992. **1**: p. 515-521.
44. Aning, A.O., Z. Wang, and T.H. Courtney. *Tungsten Solution Kinetics and Amorphization of Nickel in Mechanically Alloyed Ni-W Alloys.* Acta Metallurgica Et Materialia, 1993. **41**(1): p. 165-174.
45. Goldwasser, D.J. and B.H. Kear. *Properties of a Resin Matrix Composite Reinforced with Amorphous Metal Ribbons.* Materials Science and Engineering, 1976. **23**(2-3): p. 237-239.
46. Takayama, S. and R.G. Fehrman. *Composite Metallic-Glass Wires.* Journal of Materials Science, 1980. **15**(2): p. 532-534.
47. Cytron, S.J. *A Metallic Glass-Metal Matrix Composite.* Journal of Materials Science Letters, 1982. **1**(5): p. 211-213.
48. Ruutopold, A., R.A. Varin, and Z. Wronski. *The Role of Interfaces in the Application of Rapidly Solidified Metal Ribbons as Reinforcements for Composites.* Materials Science and Engineering, 1988. **98**: p. 547-551.
49. Stawovy, M.T. and A.O. Aning. *Processing of amorphous Fe-W reinforced Fe matrix composites.* Materials Science and Engineering a-Structural Materials Properties Microstructure and Processing, 1998. **256**(1-2): p. 138-143.
50. Abramoff, M.D., Magelhaes, P.J., Ram, S.J. *Image Processing with ImageJ.* Biophotonics International, 2004. **11**(7): p. 36-42.
51. *ASM Metals Reference Book*, ed. M. Bauccio. Materials Park, Ohio: ASM International, 1993.
52. Elomari, S., R. Boukhili, and D.J. Lloyd. *Thermal expansion studies of prestrained Al2O3/Al metal matrix composite.* Acta Materialia, 1996. **44**(5): p. 1873-1882.
53. Vaidya, R.U. and K.K. Chawla. *Thermal expansion of metal-matrix composites.* Composites Science and Technology, 1994. **50**(1): p. 13-22.
54. Chan, K.C. and J. Liang. *Thermal expansion and deformation behaviour of aluminium-matrix composites in laser forming.* Composites Science and Technology, 2001. **61**(9): p. 1265-1270.

55. Xie, X.Q., D. Zhang, and J.S. Liu. *Thermal expansion properties of TiC particle reinforced ZA43 matrix composite.* Materials & Design, 2001. **22**(3): p. 157-162.
56. Courtney, T.H. *Mechanical Behavior of Materials*. 2nd ed. Boston: McGraw Hill, 2000.
57. *Quantitative microscopy*, ed. R.T. DeHoff and F.N. Rhines. New York: McGraw-Hill, 1968.
58. Scheuer, U. and B. Lengeler. *Lattice Distortion of Solute Atoms in Metals Studied by X-Ray-Absorption Fine-Structure.* Physical Review B, 1991. **44**(18): p. 9883-9894.
59. *Interfacial phenomena in composite materials '91 : proceedings of the second international conference, held 17-19 September 1991 in Leuven, Belgium*, ed. I. Verpoest and F. Jones. Oxford; Boston: Butterworth-Heinemann, 1991.

Appendix A: Composite Yield Stress at 0.2% Strain Offset

Reinforcement Volume %	Test #	Yield Stress [MPa]
0	1	265
	2	270
	3	265
10	1	497
	2	516
	3	495
25	1	643
	2	642
	3	640
45	1	1010
	2	1039
	3	1027

Appendix B: Vickers Macro-hardness Measurements on Composite Samples

Vickers macro-hardness : 10kg							
0 vol. %		10 vol. %		25 vol. %		45 vol. %	
µm	HV	µm	HV	µm	HV	µm	HV
375	132	303	202	266	262	228	357
378	130	289	222	274	247	233	342
372	134	298	209	259	276	233	342
372	134	300	206	268	258	228	357
378	130	308	196	271	253	220	383
379	129	301	205	272	251	221	380
380	128	302	203	259	276	244	312
378	130	301	205	270	254	224	370
378	130	297	210	265	264	230	351
376	131	299	207	265	264	228	357

Appendix C: Detailed Explanation of $L_{e\text{-}e}$ Calculations with ImageJ and Mathematica

Five SEM images of each composite sample were taken at the same magnification using a backscattering detector. For each image: the scale on ImageJ was first calibrated to the micrograph, and the image was cropped to remove the SEM specifics data at the bottom. The micrograph was processed twice with Binary/Threshold. This function changes greyscale images to black and white. The white particles stay white and the grey matrix turns black. The program assumes objects are black and background is white for analysis calculations, so it is necessary to use Binary/Threshold a second time to reverse all the pixels. Thus the particles turned from white to black, and the porosity and matrix turned from black to white. This process is shown in Figure 44, Figure 45, and Figure 46 for one of the SEM images of a 25% vol. reinforced composite.

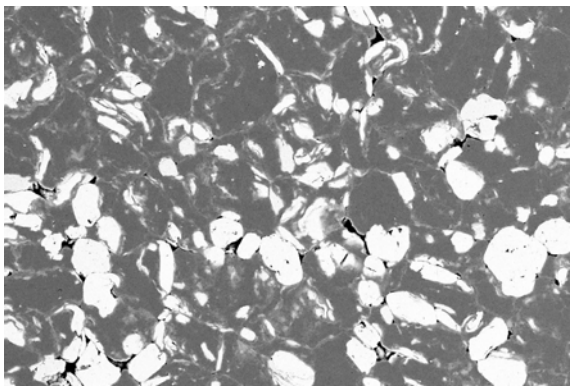

Figure 44. SEM image cropped

Figure 45. Binary/Threshold 1

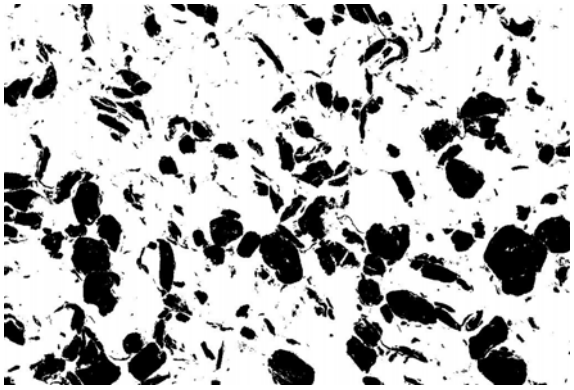

Figure 46. Binary/Threshold 2

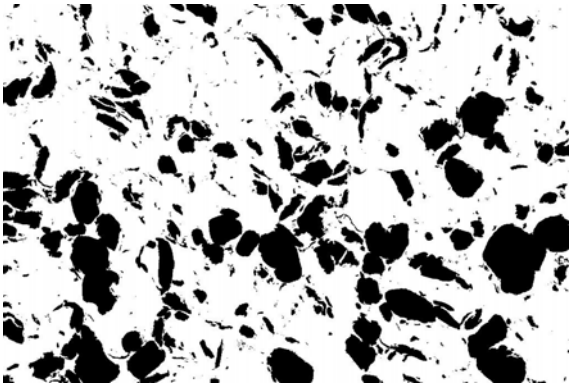

Figure 47. Mask of Figure 46

After the second Binary/Threshold is applied, it is noticeable that some of the black particles contain small white pixels. This is often not a matrix phase but an anomaly like a particle crack or polishing flaw. A final processing step called Analyze Particles/Mask was used. It draws narrow lines around all the particles and fills them in. This was done on Figure 46 to make Figure 47. As an adverse affect, some of the reinforcement particulates which were very close are drawn together as a single particle by the mask process. This is justified from a composite strengthening perspective because several particles close together behave as a single larger particle. After the SEM image was processed, ImageJ was used to draw a line and the Analyze/Plot-Profile function was used. Plot-Profile displays a two-dimensional graph of the intensities of pixels along a line within the image. All the pixels are labeled "0" for white/matrix and "255" for black/particles, and the plot-profile was saved as a text file which is a list of these pixels. Ten lines were drawn for each SEM photo and saved as text files, thus the 10, 25, and 45 vol. % reinforcement composites each had 50 lines drawn. Figure 48 below shows an example of a plot-profile graph.

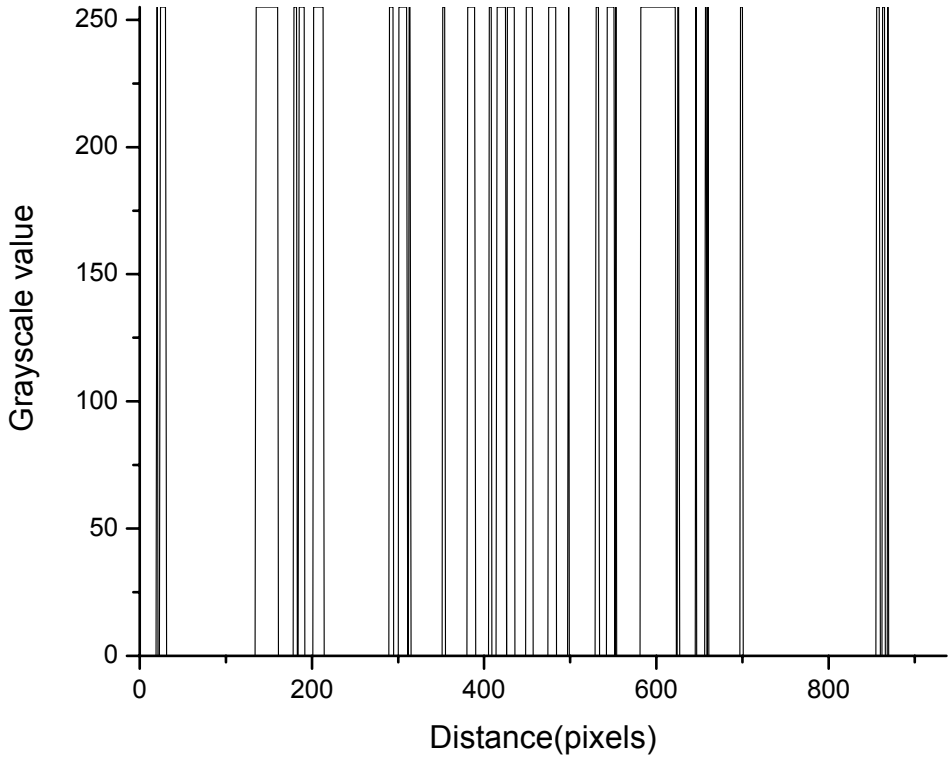

Figure 48. Example plot-profile graph of a line drawn on an SEM image using ImageJ

ImageJ can create pixel lists of plot profiles from lines on SEM micrographs, but it can not effectively analyze the lists for each matrix segment to find the average $L_{e\text{-}e}$. Mathematica is a program that is designed for quantitative calculations. Mathematica can evaluate the plot profile pixel lists created by ImageJ to yield an average $L_{e\text{-}e}$. A program was written in Mathematica to import each plot-profile pixel list text file and calculate the average length of the matrix segments the line traversed. Each matrix segment was defined in the program as every group of white pixels between black pixels and the ends of the line. A copy of this program is in Appendix D. The average matrix segment length of the 50 lines was calculated for each composite and is shown in Appendix E.

Appendix D: Mathematica Program to Estimate $L_{e\text{-}e}$

```
Off[General::"spell1"];
Off[General::"spell"];
Off[General::"partw"];

SetDirectory[$HomeDirectory];
SetDirectory["Desktop"];
SetDirectory["research"];
SetDirectory["semplots"];

threshold=0;

z=Import["45v1kx5-10","list"];

n=2;LngP=0;LngM=0;ttlP=0;ttlM=0;avgP=0;avgM=0;numP=0;numM=0;

While[NumberQ[z[[n]]]==True,{If[z[[n]]==0,{If[LngP>threshold,{avg
P=(avgP*numP+LngP)/(1+numP),numP=numP+1,Print["Particle
length/total/avg =
",LngP,"/",numP,"/",avgP//N]},LngM=LngM+1,ttlM=ttlM+1,LngP=0},{I
f[LngM>threshold,{avgM=(avgM*numM+LngM)/(1+numM),numM=numM+1,Prin
t["Matrix distance/total/avg =
",LngM,"/",numM,"/",avgM//N]},LngP=LngP+1,ttlP=ttlP+1,LngM=0}],I
f[Num-
berQ[z[[n+1]]]==False,{If[LngP>0,{avgP=(avgP*numP+LngP)/(1+numP),
numP=numP+1,Print["Particle length/total/avg =
",LngP,"/",numP,"/",avgP//N]},{avgM=(avgM*numM+LngM)/(1+numM),num
M=numM+1,Print["Matrix distance/total/avg =
",LngM,"/",numM,"/",avgM//N]}],Print["Total Particle Fraction:
",ttlP/(ttlP+ttlM)//N]},n=n+2}]

Print["Avg Le-e[um]=",z[[n-3]]*avgM/(ttlP+ttlM)//N]
```

Appendix E: $L_{e\text{-}e}$ Values Estimated by Mathematica for Each Composite

	10 Vol. % Reinforcement Le-e[um]				
	Image 1	Image 2	Image 3	Image 4	Image 5
Line 1	19.89	17.78	18.05	22.68	26.23
Line 2	47.62	29.66	37.39	48.07	38.3
Line 3	23.81	28.46	31.2	33.76	18.48
Line 4	30.14	45.86	22.51	30.18	19.55
Line 5	22.68	26.95	14.32	43.36	17.22
Line 6	43.51	21.88	16.18	22.11	33.95
Line 7	17.23	20.24	30.45	22.51	16.4
Line 8	15.7	42	23.26	37.31	43.1
Line 9	29.26	27.41	31.36	35.15	46.81
Line 10	65.7	14.74	14.97	27.68	13.96
				Avg:	**28.54**

	25 Vol. % Reinforcement Le-e[um]				
	Image 1	Image 2	Image 3	Image 4	Image 5
Line 1	15.11	10.27	11.14	20.95	11.2
Line 2	9.06	10.82	9.1	9.58	19.32
Line 3	7.89	10.69	10.75	8.37	8.57
Line 4	13.65	7.22	8.99	11.36	11.73
Line 5	12.18	10.86	14.59	10.42	9.42
Line 6	9.56	4.94	12.27	13.36	13.17
Line 7	10.74	20.36	7.87	10	13.83
Line 8	7.86	8.39	15.58	11.52	14.39
Line 9	10.51	29.55	9.46	9.16	13.26
Line 10	9.87	12.69	15.71	11.58	17.87
				Avg:	**11.93**

	45 Vol. % Reinforcement Le-e[um]				
	Image 1	Image 2	Image 3	Image 4	Image 5
Line 1	7.31	5.97	3.87	6.82	4.25
Line 2	6.85	5.38	8.49	4.17	5.15
Line 3	4	4.17	5.23	6.03	5.62
Line 4	7.09	12.78	9.03	9.32	4.37
Line 5	8.63	5.87	11.84	6.06	6.53
Line 6	6.48	9.03	4.87	5.21	5.01
Line 7	5.79	5.67	4.99	10.78	6
Line 8	5.84	4.13	4.76	5.96	5.82
Line 9	5.67	7.58	7.55	6.91	4.48
Line 10	5.05	4.22	6.92	4.33	6.41
				Avg:	**6.29**